UNIVERSITÀ DEGLI STUDI DI PADOVA
Dipartimento di Ingegneria Industriale DII
Corso di Laurea Magistrale in Ingegneria Aerospaziale
Curriculum: Aeronautico

NUMERICAL SIMULATION OF HULL INSTALLATION OF A NOVEL OUTBOARD DYNAMIC INLET WATERJET

Relatore: Prof. Andrea Magrini

Correlatore: Dr. Filippo Avanzi

Laureando: Tommaso Rossi, 2070685

Anno Accademico 2024/2025

"Success is not final, failure is not fatal:
it is the courage to continue that counts."

— Winston Churchill

"It always seems impossible until it's done."

— Nelson Mandela

ABSTRACT

The present thesis investigates the propulsive performance and the installation effects of a novel waterjet concept for sustainable marine propulsion. This innovative system is called Outboard Dynamic-Inlet Waterjet (ODW) and it features a unique operational mode, being completely submerged and benefiting from an axial dynamic inlet and propulsive nozzle. Unlike traditional waterjets, the ODW's biggest advantage is that it operates in an axial, uniform captured stream tube, resulting in higher efficiency and thrust.

The primary objective of this work is to investigate the installation of the propulsive system and its mutual effect with the hull, by analysing the dynamics and performance. A total of 13 installation locations of the engine at different submergence and longitudinal positions are studied in steady-state Reynolds Averaged Navier-Stokes equations.

Following an accurate mesh validation process, the simulations yield satisfactory results. The analysis of the Net Vehicle Force highlighted the most forward installation position as the most advantageous, where the net force coefficient exceeds the ideal value of 0.285. However, not all performance parameters are maximised in this configuration: while a reduction in hull drag is observed, the available Net Propulsive Thrust also decreases. Conversely, the worst configuration is found slightly ahead with respect to the trailing edge of the hull, at non-dimensional coordinate $(-0.7788\ ;\ -0.1657)$, where minimum performance is recorded and cavitation occurs even under design conditions.

SOMMARIO

Il seguente progetto di tesi analizza le performance propulsive e gli effetti di installazione di un motore idrogetto di nuova concezione, che pone le basi per una propulsione marina più sostenibile. Questo sistema innovativo è chiamato Outboard Dynamic-inlet Waterjet (ODW) ed ha la peculiarità di essere completamente sommerso e dotato di una presa dinamica, una pompa assiale ed un ugello che fornisce la spinta necessaria all'avanzamento. A differenza dei tradizionali motori ad idrogetto, il vantaggio di questo propulsore è di essere esposto ad un flusso in direzione assiale uniforme e "indisturbato", incrementando così l'efficienza e la spinta disponibile.

Il principale obiettivo di questo studio è quello di investigare la miglior posizione di installazione del propulsore, analizzando gli effetti di mutua interazione con lo scafo attraverso lo studio delle forze agenti sul sistema. Un totale di 13 posizioni di installazione, con diverse distanze verticali e longitudinali, sono studiate attraverso simulazioni stazionarie basate sulle equazioni di Navier-Stokes mediate di Reynolds (RANS).

Dopo un'attenta validazione delle mesh e delle simulazioni, sono stati ottenuti risultati soddisfacenti, che vengono riportati brevemente in seguito.
Dalla prima analisi effettuata sul campo di pressione, si è subito riscontrato un punto di installazione estremamente sconveniente, in cui anche in condizioni di crociera si verifica il rischio di cavitazione all'inlet e all'uscita dal nozzle.
Il secondo argomento affrontato è basato sull'investigazione delle forze di resistenza e portanza agenti sullo scafo. Da questa analisi è stato possibile individuare che la posizione di installazione che minimizza la resistenza idrodinamica corrisponde alla posizione longitudinale più spostata verso prua. L'influenza del propulsore è in questo caso benefica e permette di migliorare il coefficiente di drag dello scafo isolato fino ad un valore pari a -0.00272. Al contrario però, il motore installato in questa posizione ha effetti svantaggiosi sulla forza verticale, producendo una spinta verso il basso che può causare un incremento dell'impronta in acqua dello scafo e dunque un incremento di resistenza idrodinamica.
Il focus dell'analisi passa poi alla dinamica del propulsore, analizzando in modo principale la forza di resistenza e le performance propulsive. L'installazione sullo scafo offre un contributo positivo alla dinamica del propusore solo se posizionato nel punto di massima distanza longitudinale dalla chiglia ove si verifica una riduzione massima del C_D di circa -0.035. Le performance propulsive sono poi analizzate sotto forma di spinta netta disponibile (NPT), che risulta essere massima nella posizione in cui si verifica la minima resistenza.
L'ultima analisi si concentra invece sulla definizione della Net Vehicle Force, che tiene conto sia della dinamica dello scafo che del propulsore. Questa forza ha evidenziato che la posizione di installazione più avanzata verso prua è la più vantaggiosa, raggiungendo un coefficiente di spinta netta che supera quello di riferimento di circa 0.285. Anche la posizione di installazione più arretrata mostra buone performance, anche se con una efficienza inferiore.

CONTENTS

LIST OF FIGURES

LIST OF TABLES

1 INTRODUCTION

Thanks to the technological enhancement in the last few decades, water propulsion systems are experiencing a big change: the tendency to use contemporary waterjet propulsive systems instead of the classical propellers is increasing.
In this chapter, a brief review of the history of waterjet propulsive systems is presented.

1.1 Waterjets

Waterjets may be considered as one of the common contemporary propulsion systems, even if their origins date back to the beginning of "mechanical" navigation. This propulsion method is not as popular as conventional propellers, but in many operating conditions it is even better. The tendency to use waterjet propulsion is increasing thanks to the enhancements of these systems, which become even faster, more silent, more ecological, and with better handling than the competing propellers.
In order to investigate the reasons behind this increased interest in applying waterjet propulsion, we need to know the specific characteristics of the propulsion method and its advantages and disadvantages under various operating conditions.
In this section a brief review of the history of waterjet propulsion and its operations are presented.

1.1.1 History and applications

The first time that a waterjet appeared in the navigation world dates back to the second half of the 18^{th} century, after the invention of the steam machine. The American Founding Father, Benjamin Franklin (1706-1790), was inspired by Daniel Bernoulli to develop a new waterjet propulsion system. As reported by James Thomas Flexner (1944) who discussed the history of the steamboats, the French scientist believed that "if a stream of water was driven out of the stern of a boat below the water line, its reaction on the body of water in which the boat floated would drive the vessel forward"; so he developed an L-shaped pipe stretching to the boat's stern from which water could be expelled. The improvement made by Franklin was the addition of a pump to suck the water into the bow [1].

In 1786 John Fitch and James Rumsey began meaningful experiments using some variant of the Newcomen steam engine. Rumsey developed a tube boiler and utilised it in his waterjet system: it consisted of two cylinders, one of steam on top that moved the piston rod connected to the other one that operated the pump. This mechanism sucked the water from the bow and rushed out of the stern.
Some years later, Fitch resumed some concepts applied by Dr. John Allen; the idea was to force a column of air through the water-filled ducts to create a jet of water expelled from the stern (a valve closed the bow duct to avoid backflow). After some trials, engineers noticed that some

characteristics of this type of propulsion system were too inefficient due to the high losses caused by the friction between the fluid and the long duct walls, and handling was really difficult. The solution to this problem arrived with the invention of hydraulic pumps: they reduced the losses by obviating the need to raise or turn long ducts and aligning the centrifugal pump axis horizontally [1].

The first modern jet-boat was developed by the New Zealand engineer Sir Charles William Feilden Hamilton, who also founded a waterjet manufacturing company in the following years. His first goal was to build a boat that could navigate the shallow fast-flowing New Zealand rivers; the water level, in fact, was too low to use propellers because they would have hit the bottom of the river [5].

In recent history, an example of waterjets for military purposes was the so-called PBR (*"Patrol Boat River"*: a fluvial boat built by the Americans for the US Navy and developed to navigate as fast as possible the shallow Vietnam rivers to patrol and take control of the waterways. This boat had two Jacuzzi diesel waterjets that could reach 27 knots (about $46\ km/h$) even in the insidious Vietnamese river waters [6]. One of the characteristics of the PBR (as most waterjet boats) was its agility and the ability to stop quite instantly and in a very small space by a $180\,\mathrm{deg}$ rotation of the jet.
Nowadays, jet-boat applications include, for example, fast passenger ferries, control and rescue patrols, military boat operations in shallow water, sport activities such as jet skis, and many others.

1.1.2 Common waterjets configurations and design

A waterjet engine uses the same principles as a propeller to generate thrust: the fluid is accelerated and a difference in momentum is established between the entry and exit sections of the system.
Generally, two types of waterjet system can be distinguished and the main differences are in the geometry of the ducting channel and the type of pump installed in these devices (Figure 1.1. The most diffuse is the flush type intake, in which the intake opening is located above the hull and is orientated in a parallel way with respect to the flow; this technology is used in the widest selection of applications.
However, there is the ram (or pod) waterjet, which finds its wider application particularly in hydrofoils and in which the intake opening is normal to the intake flow. This configuration allows for undisturbed flow at the intake highlight section, but is impacted by higher losses due to the long ducts.

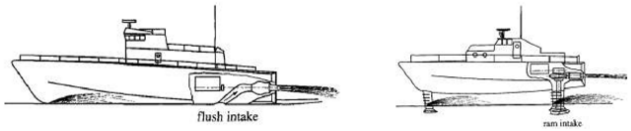

Figure 1.1: Waterjet most diffuse configuration, adapted from [1]

The most common system includes an inlet duct, a pump, a nozzle, and a steering unit: water is sucked into the intake and guided through the ducting channel into the pump composed of a rotor and a stator. The pumps are categorised into axial, mixed, or centrifugal; the first are the most popular because they can offer high performances with the smallest dimensions. After the pump, the high-pressure flow approaches the nozzle, where the momentum flux is increased due to the converging section shape. The steering device can deflect the jet in order to create steering and reversing forces. In the following picture (Figure 1.2) a standard flush-intake configuration is reported from Bulten's work on waterjet propulsion systems [2].

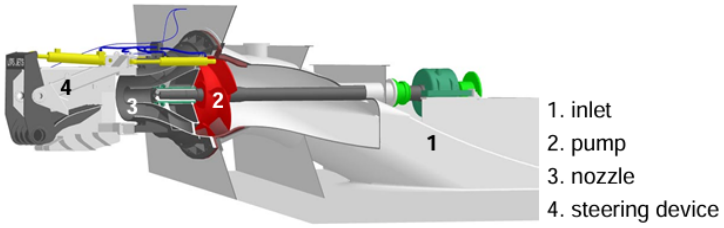

Figure 1.2: Three-dimensional view of a flush-intake waterjet installation, reported from [2]

One of the most critical aspects in waterjet development is the design of the intake because this device should avoid the occurrence of cavitation while ensuring the maximum pressure at the pump face and maintaining hydrodynamic losses at a minimum. Cavitation is one of the worst hydrodynamic phenomena that consists of the formation of vapour bubbles, which occurs when the pressure of the fluid drops below the vapour water pressure. The implosion of these bubbles that occurs when they encounter a high pressure zone, can cause several structural damages, in particular in proximity to the pump blades (Chapter 2, Section 2.4).
The cavitation problem is the major propulsive limit for open rotor design propulsive systems because their free stream tube path varies with the advancing velocity, so the flow condition at the propeller depends only on this quantity. In waterjets, instead, the shape of the ducting dictates the flow speed and hence can be advantageously used to increase static pressure on the impeller face, thus delaying or reducing the occurrence of the cavitation phenomena.
From a design point of view this is the principal difference between propellers and waterjet propulsion systems: the second ones can count on one more control over the incoming flow; thereby, they ensure the required mass-flow rate with a pressure that avoids cavitation and that optimises the pump operation.

1.2 IMPRONTA-0

1.2.1 Towards greener navigation

The present and future of navigation are headed toward an increasingly greener horizon through a progressive decarbonisation of marine transports.
The idea is to leave the internal combustion engine and encourage a more sustainable propulsion source. Research institutes, universities, and companies are developing new technologies such as electric engines powered by rechargeable batteries and the implementation of new types of fuels like hydrogen or biofuels to guarantee a greener future for navigation systems.

1.2.2 New project

"*IMPRONTA-0*" is the name of the project that involves the "Università degli Studi di Padova" and the "Università Ca' Foscari di Venezia" to investigate the effects of a new water propulsive system called Outboard Dynamic-Inlet Waterjet (ODW). This study stems from the need to renew the navigation in our Venetian lagoon, with the aim of reducing the environmental impact of current propulsive systems. This involves addressing both the water and air pollution caused by fossil fuels and the impact on marine biology.
The project focusses on "the feasibility of the actual use of this propulsion system in Venice. Integrating this innovation into the lagoon environment requires a specific analysis of technological adaptation and economic impact. Therefore, we have investigated the best technical configuration based on different uses, aiming to understand the necessary investments, supporting policies, and services, such as a charging network for boats. All of this has been considered in light of the significant benefits in terms of reducing noise pollution, pollutant emissions, and wave motion.", as explained by the Ca' Foscari University of Venice's Professor Raffaele Presenti [7].
In line with European directives and regional strategies for energy transition, in fact, the ODW is powered entirely by environmentally friendly energy sources, such as electric or hybrid motors, or green fuels such as hydrogen.

1.2.3 Outboard Dynamic-Inlet Waterjet design

The IMPRONTA-0 propulsion system operates on the principle of action and reaction, where the thrust required to move the vessel results from the reaction to the force generated by the expulsion of a water jet. Water is drawn in through the intake and directed into the axial pump, where the internal rotor-stator stage transfers the energy of the engine to the fluid. Finally, high-pressure water is accelerated and expelled through the nozzle, generating propulsive thrust.

The design of the Outboard Dynamic-Inlet Waterjet (ODW) follows the guidelines of an aeronautical propulsion system. The knowledge gained about the behaviour of axial compressors used in aeronautics has inspired the idea of applying this technology to waterjets, despite the following fundamental differences: the reference flow is the water, an incompressible fluid, so the flux velocity does not depend on compressible phenomena like shock waves but on the formation of cavitation bubbles; the blades, designed to work in a liquid, have completely different mechanical problems with respect to aeronautic compressors' blades: in the first ones, in fact, bending stresses dominate over normal centrifugal stresses.
Like an aeronautical propulsive system with no turbine, the ODW comprises a single device that includes the dynamic intake, the pump, and the exhaust nozzle. This technology requires no shaft to drive the rotor, so no additional supplementary components such as gearboxes or steering systems are added to the system and no obstructions affect the entering flow. Moreover, this type of propulsion system, being a fully segregated propulsion device, has another unique aspect: it can be "simply" studied as an isolated body immersed in a fluid.
Another big similarity of this propulsor with an aeronautical one is that it is completely exposed to the 'undisturbed' flow, which perpendicularly enters into the inlet, reducing the mass losses, and remains aligned with the thrust direction, with no oblique stream evolution and much less duct friction compared to a ram waterjet.

1.3 Motivation and objectives

Although waterjet propulsion origins can be traced back many centuries ago, they are still considered a relatively modern technology: in fact, they have only started to become a common water propulsive system a few decades ago.
Over the years, in fact, there has been a tendency to employ marine screw propellers rather than waterjet systems. The reason is that the design and production procedures for this type of propulsion systems are easier.
However, the introduction of more efficient pumps changed this trend, and nowadays some specific characteristics of waterjet propulsors make them a better choice in comparison with conventional marine propellers.
The first waterjet applications were developed for military purposes, so the documentation remains classified and inaccessible. Together, these factors contribute to a rather limited and not particularly detailed scientific literature on the functioning of these devices, whose physics still leaves room for significant questions and uncertainties.
In addition, the heart of the "IMPRONTA-0" project, the Outboard Dynamic-inlet Waterjet, represents an innovative approach which further explains the lack of available experimental data in the scientific literature, making the investigations on the ODW extremely intriguing from a scientific perspective. In fact, this project can lay a solid foundation for the advancement of a technology that is still open to new discoveries.
These are the words of Professor Ernesto Benini, scientific project leader and creator, who ex-

plains the advantages of this innovation: "Compared to conventional propellers, the system's architecture makes it extremely quiet and free from annoying vibrations. Moreover, the system is specifically designed to be paired with electric and hybrid engines, which are essential for clean navigation with minimal environmental impact. Unlike traditional waterjets, this propulsor features a fully outboard configuration, allowing for easy installation on boats operating in the Venetian lagoon without requiring hull modifications. The high thrust typical of waterjet propulsion, combined with the instant torque of the electric motor, gives this system remarkable responsiveness and manoeuvrability right from the first revolutions of the engine, ideal for navigating the busy canals of the lagoon.", [7].

A large compendium of numerical methods can be found in the document [8], in which many aspects of this new isolated technology are investigated.
To achieve results that are both accurate and as realistic as possible, additional investigations are necessary, such as evaluating the effects of installing the propulsor on the hull.
The hydrodynamic interaction established between the hull and the propulsive system is not a new concept in navigation: even the propellers need similar analyses to investigate these phenomena that influence the propulsive efficiency and so the propulsor design. As explained by G. Trincas [9], the velocity field that hits the propeller is influenced by the presence of the hull and therefore propulsion is affected by its shape, but also the pressure field around the hull is influenced by the presence of the propeller in a mutual body interaction.

This thesis specifically revolves around the installation phenomena of the new propulsion system that is analysed under two operating conditions: under the design cruise velocity and another at lower speed, to investigate hull's boundary layer ingestion phenomena. Furthermore, an optimisation study will be carried out regarding the ideal placement of the engine on the hull and the hull-propulsor interaction, drawing inspiration from studies conducted in the field of aeronautics.

The analysis of installation effects is a fundamental study aimed at maximising overall system performance. Phenomena such as boundary layer ingestion, cavitation onset, and the thrust generated by the propulsor are strongly influenced by the presence of the hull and the engine's installation position relative to the hull.
Performance improvements can arise, for example, from an increase in thrust generated by a more stable flow entering the axial pump, or from a reduction in drag on the walls of the propulsor or the hull, leading to lower energy consumption and increased autonomy of this new technology.
The variation in the position where the ODW is installed, being fully exposed from the hull, does not require major modifications to the hull or high installation efforts. Therefore, the benefit of optimising these results translates into a performance gain at no additional cost, without altering the components of the propulsor. This feature makes the study conducted in this thesis essential.

1.4 Thesis Structure

After a brief historical reference in Chapter 1, in which waterjet evolution is reported, a quick description of the latest waterjet propulsion systems is given. The following Chapter 2 analyses the methods used to complete the investigation about the hull installation of the Novel Outboard Dynamic Inlet Waterjet, including the theory of waterjet/hull interaction, the numerical methods used for the simulations, and the geometry in exam. In Chapter 3 the results obtained from the simulations are investigated, processed, and then reported and analysed through explicative figures. In the last chapter, the conclusions extracted from the analysis computed in all other sections are collected.

2 METHODS

In the following sections, the methods applied to compute these project results are investigated, with brief theoretical references that can help to understand the problem.

2.1 CFD models for simulations

In the last few years, the use of numerical simulations to approximate the behaviour of physical, mathematical, or engineering systems has increased exponentially due to the advancement of computational resources.
The science that deals with solving the complex fluid flow governing equations is called Computational Fluid Dynamics (CFD), and it uses methods like finite differences, finite volumes or finite elements to approximate the fluid motion and give some fast and economical results.
The computational methods adopted in the whole study are based on the solution of steady RANS - Reynolds Average Navier-Stokes - equations in numerical models of different complexity. For all simulations, the commercial flow solver Ansys Fluent [10] solves the characteristic fluid equations in every cell that composes the mesh fluid domain in every time interval. The spatial and temporal discretization introduce some errors that depend on the case and on the discretization order, and that move the numerical solution away from the analytical one. Numerical methods need to satisfy three fundamental properties in order to achieve an acceptable solution:

- consistency: the approximate solution must tend to the analytical one with decreasing of spatial and temporal discretization intervals;
- stability: the error between the approximate and exact (analytical) solution must stay bounded in a certain interval;
- convergence: the numerical solution must tend to the approximate one with decreasing of spatial and temporal discretization intervals;

The most diffuse method used to solve fluid problems is the Finite Volume Method (FVM), which briefly consists in discretising the computational domain into many nodes, which lie in a small volume that does not overlap with the surrounding ones and is called "cell". The whole cells in the computational domain make the mesh, which is probably the most important tool to obtain acceptable results from the simulations.
The finite volume method provides modelling capabilities for a wide range of cases: incompressible and compressible, laminar and turbulent, single-phase and multi-phase fluid flow problems, and structured and unstructured mesh can be solved. Fluent is one of the most diffuse software that, thanks to its flexibility, suits even with the most complex industrial problems.
The characteristic equations are solved at every discrete point, in time intervals that depend on the temporal discretisation method, to determine the flux variables at that position and at a certain time. The domain discretization is an intrinsic issue in the FVM because the numeric

solution is computed only at one point of the cell (corresponding to the node), at which the mean approximated value is known $\vec{\overline{U}}_i$. To determine the flux across the control volume boundary, which allows the calculation of the solution in the adjacent cell $\vec{\overline{U}}_{i+1}$, a predefined distribution of the variable must be assumed within the computational mesh.
A first-order distribution is defined when the variable is considered constant throughout the cell, which means that the nodal value is assumed to be uniform throughout the entire volume. A second-order distribution assumes, instead, a linear variation of the variable within the cell, while higher orders account for non-linear distribution of the value with increasing complexity.

2.1.1 Governing equation

The Navier–Stokes equations are a system of coupled partial differential equations that describe the fluid dynamics in an absolutely exact way. In this thesis, the working fluid is water, which behaves as an incompressible fluid, for which the density, ρ, is constant throughout the entire domain.
By considering this assumption in the complete Navier-Stokes equations, the system is simplified in the form shown in Equations 2.1. This version describes the dynamics of an incompressible fluid and consists of four conservation equations: one for mass (continuity) and three for momentum. The conservation of energy is not considered, since it is typically relevant only in compressible flows, where the density plays a significant role, adding an additional variable. To solve the system and the closure problem of these non-linear equations, constitutive relations must be introduced. However, despite extensive studies, a general analytical solution to the Navier–Stokes equations remains unsolved.
As a result, the only practical approach to obtaining realistic and time-efficient solutions is through the use of numerical methods and modeling approximations in Computational Fluid Dynamics (CFD). These simplifications inevitably introduce errors into the results, which is why CFD simulations must always be validated by the comparison of the solutions against experimental data or, when not available, with other verified numerical results.

$$\begin{cases} \vec{\nabla} \cdot \vec{V} = 0 \\ \rho\Big(\frac{\partial \vec{V}}{\partial t} + \vec{V} \cdot \vec{\nabla}\, \vec{V}\Big) = -\vec{\nabla} p + \rho \vec{g} + \mu\, \nabla^2 \vec{V} \end{cases} \tag{2.1}$$

where $\vec{V}$ is the velocity vector, composed by the three direction components (u, v, w); ∇p represents the pressure variation for each momentum equation; μ is the dynamic viscosity and the term $\mu\, \nabla^2 \vec{V}$ represents the viscous diffusion of the velocity. This term is fundamental when the viscosity effects have to be taken into account, in particular in high velocity gradient zone. The last term, $\rho \vec{g}$, describes the inertial forces.
The strong intrinsic non-linearity of the system is responsible for the fundamental fluid criticalities like turbulence, multi-scale vorticities, and non-stationary phenomena.

2.1.2 Turbulence modelling

Turbulence is the three-dimensional unsteady random motion observed in fluids at moderate to high Reynolds numbers. As technical flows are typically based on fluids of low viscosity, almost all technical flows are turbulent. One of the fundamental aspects, as well as one of the most critical aspects of fluid dynamic analysis, is the computation of turbulence.
It is practically impossible to solve industrial or complex engineering problems by Direct Numerical Simulations (DNS), in which all turbulence scales are resolved, because the necessary computational resources are too vast. So, averaging procedures have to be applied to the Navier-Stokes equations to filter out the turbulent spectrum. The most widely applied averaging procedure results in the Reynolds-averaged Navier-Stokes (RANS) equations, in which the flow variables are split into a mean and a fluctuating part, avoiding all turbulent structures from the flow and obtaining a smooth variation of the averaged velocity and pressure fields.
These are the principles and methods on which all the thesis simulations are computed. The applied turbulence model is the default SST $k-\omega$ model (Shear-Stress Transport) that is adequate for most engineering flows because it combines elements of the ω-equation (good for near-wall flows) with the ϵ-equation (good for free-stream interactions) [10].
In CFD, the $k-\omega$ turbulence model is directly linked with an important parameter defined as:

$$y^+ = \frac{\Delta s \, U_{fric}}{\nu} \tag{2.2}$$

where Δs is the normal distance from the wall and the first mesh volume cell center, $U_{fric} = \sqrt{\tau_w/\rho}$ is the friction velocity and ν is the kinematic viscosity.
The wall y^+ is a parameter that can be extracted from the simulations, and it is fundamental to define whether the boundary layer (the fluid zone closest to the wall) is modelled or resolved by the software. The following convention is assumed:

- if $50 < y^+ < 500$ the software models the boundary layer with a wall function to connect log-low with the viscous sublayer;
- if $y^+ < 1$ the boundary layer is resolved and the highest simulation accuracy is reached.

Obviously, the application of a wall $y^+ < 1$ is much more expensive for computational resources, but it allows obtaining the most realistic results.

2.1.3 Simulations settings for convergence

The simulations are set using a common baseline, which is then modified and adapted case by case to achieve convergence. In the analysis, convergence is reached when the residuals of the continuity, velocity, kinetic energy, and omega equations reach the order of 10^{-6}. The residuals correspond to the difference between the solution calculated at step i and that at step $i-1$ and they are automatically computed by the simulation software Ansys Fluent. At the same time, two additional user-defined parameters must also converge: the hull drag and the total drag coefficient of the waterjet. A typical example of residuals' convergence is shown in Figures 3.1

and 2.5, respectively.
Since the computational grid is a hybrid structured-unstructured mesh, the Weighted Least Square is used as the gradient reconstruction method, while for pressure-velocity coupling the coupled scheme is chosen as the default one.
The pressure, momentum, kinetic energy, and dissipation terms are initially discretised using first-order upwind schemes until approximate convergence is achieved and the simulation does not diverge. Subsequently, the accuracy is switched to second-order schemes for nearly a thousand iterations, and, in the end, the momentum and turbulence terms are computed with third-order discretization until the convergence is reached.
In some cases, even the *pseudo-time-step* is used to stabilise the solution, introducing an artificial time-step to update the solution faster than the classic iterative method, and thus improving the stability and reducing the numerical oscillation.

An other particular, and even weird, strategy is about starting simulating with a number of cores between 18 to 24 instead of using an entire node of 48 processes, and this method had to be applied in almost all of the mesh to avoid the divergence of the residual. Then, once the solution starts to converge and is stabilised, it is possible to switch to 48 processes that speed up the calculation.

2.1.4 Computational Resources: HPC

The simulations completed in this thesis project are carried out at the CINECA High Performance Computing (HPC) facility, the largest computing centre in Italy and one of the largest in Europe. It was established in 1996 in Casalecchio di Reno, Bologna, after twenty years of development, to face the need to support the Italian scientific community with powerful supercomputing. Today, it is the reference point for Italy's national academic and research community because it enables world-class scientific research by operating and supporting leading-edge supercomputing technologies and managing a state-of-the-art and effective environment for different scientific communities. CINECA is one of the Large Scale Facilities in Europe for HPC and is a hosting site for some of the most powerful European supercomputers of level *Tier-0*, the highest one.
LEONARDO and *MARCONI*, are two *Tier-0* EuroHPC supercomputers hosted by CINECA that are in the first 20 positions in the "Top500" list, in which the most powerful supercomputers in the world are classified.
The simulations computed in this project are carried out using *GALILEO100*, a "Tier-1" infrastructure for scientific research made up of 554 nodes with two *Intel CascadeLake* CPUs, each with 24 cores, 2.4 GHz, and 384 GB RAM DDR4. This hardware structure allows simulating very heavy problems in much less time by using 48 processes that allow for a large parallelisation of the domain. [11]

2.2 Thrust-Drag Bookkeeping

Following the aeronautically-inspired nature of the Outboard Dynamic-inlet Waterjet, the propulsive performances are borrowed from the aero-engine Thrust-Drag Bookkeeping. The following method is based on the study of in-flight thrust measurements for turbofan engines, but it can be imported for the analysis of the waterjet model.
At the outset of a discussion of thrust and drag bookkeeping, a clear distinction between the force on a part of a body and the drag of that part of the body must be made. The d'Alembert paradox and Prandtl theory affirm that the net force on a closed non-lifting body in isolation in infinite subsonic potential flow is zero. Prandtl extended this theory to semi-infinite or infinite body, which in the streamwise direction also has zero net force. The only forces acting in potential flow would be the normal pressure forces, and there will be no friction.
Thus, the walls of an infinitely long streamtube would experience no net force either outside, since it could represent an infinite body, or inside, since pressures on either side of a streamline are equal. However, if one considers a part of either a closed body or an infinite body, then the force due to normal pressures will be non-zero. So, it is possible for a part of a body to experience a stream force that is not a drag; the force would be cancelled by equal and opposite components elsewhere on the body [12].
All bodies moving through in real flow experience a force that opposes their motion and that must be overcome to enable the movement. This force is called "drag", it is defined as:

$$D = \frac{1}{2}\,\rho\, V_{\infty}^{2}\, A_{ref}\, c_d \tag{2.3}$$

and it comprises two components, the skin friction, which is the integrated shear stress at the wall due to the fluid viscosity, and the pressure or form drag, arising from the modification of the pressure distribution due to boundary layer growth. As the drag in a potential flow is zero, the pressure drag in real flow can be expressed as the difference between the integrated pressure force in real flow and the integrated pressure force in potential flow, considering the same body shape in both cases. This concept is useful when considering parts of bodies because, as stated above, the integrated pressure force on part of a body in potential flow would be non-zero. Thus, the pressure drag will be the difference between the non-zero integrated pressure force in potential flow and the integrated pressure force in real flow.
According to a conventional assumption the flow domain is split into two regions: a drag domain and a thrust domain, and it is represented by a stream tube in which the ODW is truncated at the axial-pump out-plane. This system is shown in Figure 2.1 in which drag and thrust are separated according to the injected/ejected stream tube: everything inside is recorded as thrust while everything outside the stream tube is recorded as drag.
The forces acting on the thrust domain are indicated with θ, while the forces acting on the drag domain are indicated by ϕ. The gauge stream forces FG are evaluated in the characteristic engine sections and upstream and downstream of the boundaries of the streamtube. They act on the wall of the streamtube and they are calculated directly in the CFD-Post software by the

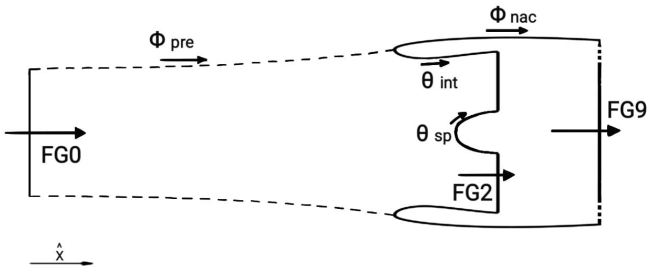

Figure 2.1: Definition of forces on a part of the isolated propulsive system model for thrust/drag bookkeeping analysis, adapted from [3]

.

computation of their expressions along the unit flow vector $\hat{x}$:

$$\phi, \theta = \hat{x} \iint \left[(p - p_\infty)\hat{\mathbf{n}} + \bar{\tau}_w \cdot \hat{\mathbf{n}} \right] \, dA \tag{2.4}$$

$$FG = \hat{x} \iint \left[(p - p_\infty)\hat{\mathbf{n}} + \rho V(\tilde{\mathbf{V}} \cdot \hat{\mathbf{n}}) \right] \, dA \tag{2.5}$$

where $\hat{n}$ denotes the surface normal, $p0$ the freestream static pressure, and $\bar{\tau}_w$ the viscous stress tensor.
By computing the momentum balance along the direction $\hat{x}$ of the streamtube in 2.1 the resulting drag is expressed like:

$$D_{nac} = \phi_{pre} + \phi_{nac} + \cancel{\phi_{post}} \tag{2.6}$$

where the first term ϕ_{pre} is the pre-entry force, the second ϕ_{nac} is the force acting on the external cowl, and the third ϕ_{post} is the post-exit force [3] that is not included in this domain. The force can be made non-dimensional by inverting the equation 2.3 by using the reference area and the freestream dynamic pressure:

$$Cd_{nac} = \frac{D_{nac}}{0.5\,\rho\,V_{ref}^2\,A_{ref}} \tag{2.7}$$

The pre-entry stream tube drag component results from the momentum balance as:

$$\phi_{pre} = FG_2 - FG_0 + \theta_{int} + \theta_{sp} \tag{2.8}$$

The nacelle inflow characteristic is associated with the non-dimensional parameter Inlet Velocity Ratio 2.18 that changes according to the operational point: it starts from values greater than one during take-off operations to decrease around 0.85 at the design point.
In aeronautics, the Net Propulsive Force can be expressed as the momentum change from the upstream infinite section 0 to the downstream infinite section:

$$Net\ Force = FG_{00} - FG_0 - (\phi_{pre} + \phi_{nac} + \phi_{post}) \tag{2.9}$$

Substituting Eq. 2.8:

$$Net\ Force = FG_{00} - FG_2 - (\theta_{int} + \theta_{spin} + \phi_{nac} + \phi_{post}) \tag{2.10}$$

Writing the momentum conservation for the post-exit streamtube you obtain:

$$FG_{00} - FG_9 = \phi_{post} \tag{2.11}$$

By isolating the term $FG_{00} - \phi_{post}$ and substituting, you get the equation for the Net Force:

$$Net\ Force = FG_9 - FG_2 - (\theta_{int} + \theta_{spin} + \phi_{nac}) \tag{2.12}$$

Then it is possible to define the Intrinsic Net Thrust (INT) as the sum of gauge stream forces at the boundaries:

$$INT = FG_9 - FG_2 \tag{2.13}$$

Considering the sum of wall forces as the "Nacelle Force" from the aeronautic world:

$$NF = \theta_{int} + \theta_{spin} + \phi_{nac} \tag{2.14}$$

the Net Propulsive Thrust becomes:

$$NPT = NF - INT \tag{2.15}$$

Equation 2.15 is suitable to be used in CFD because it allows to evaluate the Net Propulsive Force of a jet by considering only the gauge forces on the surfaces where the engine boundary conditions are applied, without calculating ϕ_{pre} and ϕ_{post} terms by the streamtube integration [3].
This equation also leads to understand the direction of force application: in a system with the engine rotation axis directed towards the stern, a negative NPF means a forward thrust and vice-versa.
In the end, the force referred to the whole submerged boat is called the Net Vehicle Force, and it considers also the effects of the other object in the system (only the hull in the present case). For the reported case, it is expressed as:

$$NVF = NPT + \phi_{hull} \tag{2.16}$$

In addition, when momentum imbalance is integrated over the whole control volume, from [8] the net thrust results as:

$$T = FG_0 - FG_9 + D_{nac} \tag{2.17}$$

2.3 Boundary Conditions and parameters

Before treating boundary and operating conditions, it is necessary to introduce the Inlet Velocity Ratio (IVR) that is defined as the ratio between inlet highlight and the free stream velocity:

$$IVR = \frac{v_{hl}}{v_\infty} \tag{2.18}$$

This fundamental parameter quantifies the shape of the captured streamtube and it defines the operating point.
An IVR value around 1 identifies a captured stream tube with a perfectly cylindrical shape, and it corresponds to the optimal configuration for cruise condition. Lower values are commonly used to identify the design point: in this condition, the captured stream tube assumes a divergent shape and a pre-diffusion takes place, with a displacement of the stagnation point on the lip toward the intake; this value must not go below a certain value to avoid external intake cavitation and a consequent increase of drag.
Conversely, values of $IVR > 1$ correspond to the start operating point or low-speed motion, in which the captured stream tube assumes a convergent shape. High IVR values can cause cavitation bubbles in the internal intake lip and cause significant damage to the pump face.
An other essential parameter in fluid dynamics is the Reynolds number, a non-dimensional quantity that defines the ratio between the inertial and viscous forces:

$$Re = \frac{\rho V_\infty L}{\mu} \tag{2.19}$$

where $\rho = 1025\ kg/m^3$ is the fluid density, v_∞ is the flow velocity $[m/s]$, L is the characteristic length $[m]$ and $\mu = 0.001077\ kg/(m \cdot s)$ is the dynamic viscosity. At low Reynolds numbers, viscous forces are dominant and the flow is characterised by smooth, constant fluid motion, whereas for high Reynolds numbers the flow is chaotic and dominated by inertial forces that produce eddies, vortices and other flow instabilities. In the actual study, the Reynolds number refers to the ODW highlight, so the characteristic length is the highlight diameter of the scaled propulsive system geometry, and it is called highlight diameter-based Reynolds number.

The analyses conducted over the whole project focus on two different operational configurations:

- the start or typical low speed off-design condition with an $IVR \simeq 1.425$ and highlight diameter-based Reynolds number $Re_{hl} = \rho v_\infty D_{hl}/\mu \simeq 2 \cdot 10^6$ obtained with a velocity of $7\ m/s$;
- the cruise or design condition with an $IVR \simeq 0.85$ advancing on a flow with $Re_{hl} \simeq 4.6 \cdot 10^6$ with a velocity of $16\ m/s$.

These two operating conditions are chosen by the analysis of the hull drag curve superimposed on the jet map in Figure 2.2, in which the Net Propulsive Thrust (NPT) curves are represented with respect to the feed velocity for different pump rotational speeds. On each curve the IVR is also reported, depending on the cruise speed, while the superimposed red line represents the drag curve of a planing hull, computed from [13].
Unlike a classical parabolic drag trend, its non-monotonic behaviour can be explained by dividing the curve into three distinct regions, each one corresponding to different cruise conditions:

- the first region is characterised by a steep increase of the drag with rising speed, culminating in a local maximum, known as the *hump* point. Physically, it corresponds to the

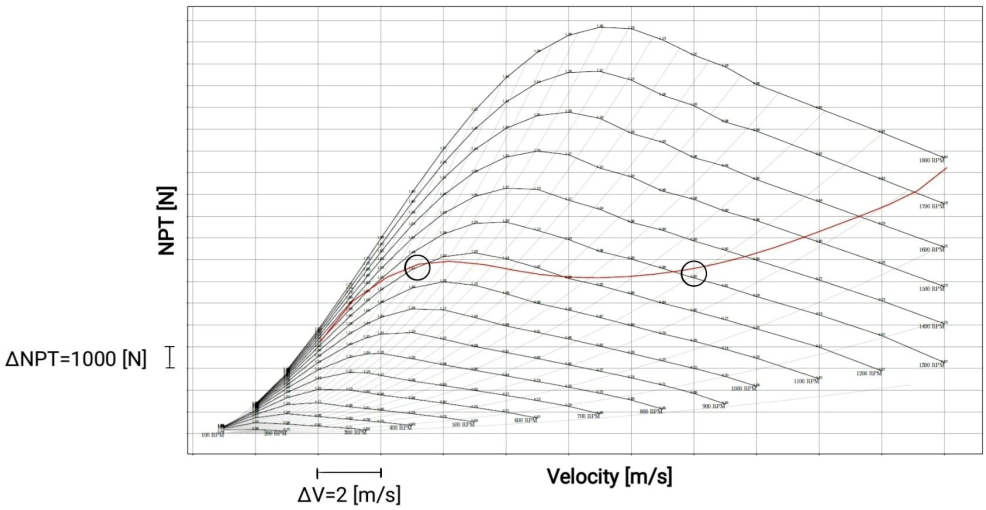

Figure 2.2: Performance map of the propulsor for different RPM on which is superimposed the real drag curve of the hull, adapted from "IMPRONTA-0" previous project.

point of maximum resistance as a result of the growth of the bow wave. This region is particularly important from a propulsion perspective, since the transition to an optimal cruising condition with enhanced performance requires overcoming the hump; to achieve this, the available net propulsive thrust must overcome the hull drag at its local maximum. It is plausible that the thrust required during steady cruising is lower than that needed to overcome the resistance of the bow wave.

- The second region corresponds to the most favourable condition, in which the trend reverses with a decreasing drag while the speed increases. Physically, this phenomenon is driven by two main factors: first, the bow wave is finally overcome and no longer impede the hull's motion; second, the hull itself is designed as a planing type, meaning that as the speed increases, its wetted surface area reduces because the bow tends to lift, lowering the drag.
- The third last region starts at the following inflection point and continues as the speed increases. This phase exhibits the typical quadratic rise in drag, characteristic of high-speed regimes. It is usual to find the cruise point at the beginning of this drag section.

Once the propulsor map has been defined, it is possible to explain the two boundary conditions chosen for the analysis of the effect of engine installation position. The low-speed off-design point is located near the *hump* point, the most unfavourable condition that must be overcome to reach more favourable conditions. The cruising point is then set at a speed of $16\ m/s$, corresponding to the region of the drag curve characterised by the quadratic trend. From Figure 2.2 it is possible to observe that the listed conditions have a comparable Net Propulsive Thrust.

2.4 Cavitation

A phenomenon that cannot be ignored in hydrodynamic and water engineering applications is cavitation. The hydrodynamic cavitation occurs when the static pressure of a liquid reduces below the saturated vapour pressure of the liquid, leading to the formation of small vapour-filled cavities, called "bubbles", in the liquid's low-pressure zones. These bubbles then follow the fluid flow until they reach higher-pressure zones, where they collapse. The implosion of these "particles" can lead to severe consequences that can even bring to system failures. The shock waves generated by the rapid vapour bubble collapse can result in mechanical (impact) damage on surfaces [14]. In this process, high internal temperatures, high pressures, and high-intensity turbulence occur, causing the erosion of the surrounding surfaces.
For the propulsor under investigation, cavitation can be particularly problematic, as it may lead to a series of potentially catastrophic consequences for its proper operation. As analysed in the dedicated section, the regions where cavitation is most likely to occur are those near the inlet highlight under low-speed off-design conditions.
The formation of vapour bubbles, besides causing potential wear by eroding the propulsor walls, leads to a chain of effects that may ultimately result in total engine failure.
Firstly, cavitation causes a reduction in the mass flow entering the axial pump. As a consequence, the compressor blades operate under off-design conditions, causing the flow incidence to increase while the mass flow rate decreases. A higher angle of incidence on the blades results in stronger pressure drops on the suction side, potentially lowering the local static pressure below the vapour pressure, promoting the formation of cavitation bubbles on the delicate hydrodynamic surfaces of the pump blades. The degradation of these surfaces can rapidly compromise their performance and may eventually lead to pump stall.
The rising flow incidence on the blades, caused by the mass flow reduction, further increases flow separation along the profiles, leading to a thickening of the turbulent wake. As a result, the pump's ability to process the incoming flow diminishes, pushing the system towards a choking condition, where the inlet flow effectively becomes "blocked". This condition leads to significant energy losses and may also trigger additional disturbances in the dynamic intake, further increasing cavitation. This creates a self-powered loop that can ultimately drive to the complete failure of the propulsion system.

2.5 Mesh and geometry

To solve the numerical simulation with the FVM in Fluent, it is necessary to discretise the geometry domain in a number of cells depending on the degree of approximation: for instance, a good approximation has a higher number of smaller cells, but they require many more computational resources.
The geometry mesh is probably the most important tool in a CFD analysis as it largely influences the behaviour of the simulations. Bad meshes can lead to divergence in very few iterations, or worse, they can give converged but completely wrong or non-physical results.

In this study, a meshing solver was employed for the generation of high-quality computational grids, ensuring accurate spatial discretisation of the domain. Its advanced meshing capabilities allowed for precise control over grid refinement, boundary layer resolution, and cell quality, which are essential for reliable numerical simulations. The software's structured and unstructured meshing techniques were used to optimise grid convergence and minimise numerical diffusion, thus improving the accuracy of computational results.
A structured grid features a repetitive pattern that can achieve high levels of quality due to its ordered connected cells, which provide the best results. In contrast, unstructured grids do not follow a repetitive pattern and are often generated automatically using space-filling algorithms. This makes the mesh generation process significantly faster, but also more difficult to modify manually. Moreover, unstructured grids do not align as well as structured grids with the flow direction, leading to a lower degree of accuracy for directional flow cases.

Initially, two different geometries are considered and separately analysed: the three-dimensional draft (corresponding to the submerged part of the hull) and the bi-dimensional waterjet geometries. The third case corresponds to the hull installed propulsor, on which the thesis project is based. These geometries are included in a large fluid domain to ensure the steadiest possible condition at the boundary, permitting the flow to dissipate all the turbulence structures and ensure a solution as stable as possible.
One of the main characteristics of the new Outboard Dynamic-inlet Waterjet is the possibility of analysing the isolated engine and the isolated hull.

2.5.1 Mesh characterisation

Since the mesh is one of the fundamental elements in a CFD analysis, it is essential to perform evaluations to ensure high-quality standards in terms of grid metrics. One of the key parameters is the mesh size, defined by the number of cells, which cannot be chosen arbitrarily. For a convergent numerical method, the numerical error decreases asymptotically as the number of cells increases, with a rate dependent on the order of convergence of the method.

Grid refinement

The process of increasing the number of cells by reducing their size is known as *grid refinement*. This method enhances the mesh resolution but can significantly increase the computational demands. As the number of cells and nodes grows, the number of systems of equations that the processor must solve increases. Conversely, a mesh that is too coarse, with widely spaced nodes, speeds up the simulation but introduces significant numerical errors. These occur because the solver fails to resolve sharp gradients properly, causing numerical diffusion and loss of accuracy in localised effects, leading to the omission of phenomena such as cavitation.
The grid refinement process is computed using an automatic script. Once the refinement factor is selected, the script can be executed to refine the mesh.

Mesh analysis

The first investigation for the definition of a good mesh is to analyse the geometry of the cell by identifying some characteristic parameters. This procedure can lead to find hard convergence zones or areas affected by high errors.
The two main grid metrics parameters are analysed:

- Aspect Ratio: in case of structured mesh with rectangular cells, it defines the ratio between the cell's length and height, so his value approaches 1 for perfectly square cells. Near walls, where the boundary layer needs to be resolved, the aspect ratio becomes very high, resulting in elongated and extremely thin cells. Despite this, the aspect ratio should ideally not exceed 10,000, depending on the solver constraints.

- Equiangle Skewness: this metric represents the deviation of the internal angles of a cell from their ideal values ($90\,\mathrm{deg}$ for quadrilaterals, $60\,\mathrm{deg}$ for triangles), defining the degree of distortion. A low skewness value indicates a minor distortion, with a skewness of zero corresponding to a perfectly quadrangular cell that minimises numerical error. In general, a well-defined mesh should maintain a maximum skewness below 0.9 to avoid instability or divergence in the solution.

Mesh sensitivity

Once the geometry has been analysed and validated through the evaluation of key mesh parameters, the mesh sensitivity analysis, also known as a grid convergence study, must be performed. This is a fundamental investigation to assess the influence of spatial discretisation and ensure solution convergence with increasing refinement. It involves analysing specific characteristic values, such as drag coefficient or pressure distribution, obtained from simulations with different refinement factors. Careless mesh sensitivity evaluations would introduce gradient errors within the sensitivity module, therefore, infecting the overall optimisation process. The development of an efficient and reliable mesh sensitivity module appears to be essential. A good mesh must have a sufficient number of cells to ensure numerical accuracy while maintaining reasonable agreement with the experimental data, without excessively slowing down the simulation. This can be achieved through a compromise between the number of cells, their size, and the level of approximation attained. In line with the convergence property, increasing the mesh resolution should ideally lead to a mesh-independent numerical solution. In reality, once a good quality mesh is set up, the results tend to flatten around an asymptotic value, demonstrating that the convergence is reached and that a further mesh refinement would be useless, as Figure 2.3 represents.
The grid refinement process is useful to find the mesh with the lowest number of cells that guarantees the best possible results.

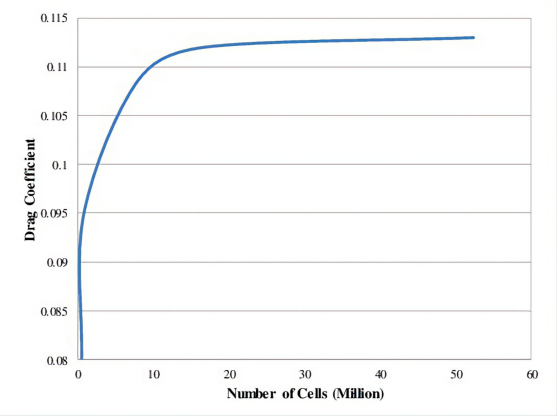

Figure 2.3: Convergence to an asymptotic value of the numerical solution with increasing number of cells, reported from [4]

2.5.2 Outboard Dynamic-inlet Waterjet

The Outboard Dynamic-inlet Waterjet mesh is the only one with a 2D geometry and is composed of five different main parts: the internal intake and nozzle (respectively before and after the pump), the external intake and nozzle that create the waterjet case and the spinner.
The mesh analysis and the mesh refinement have already been completed in previous studies, and so the results are taken into account in this work.
The mesh represented in Figure 2.4 is the only completely structured mesh that is obtained by the division of the domain into different sections; this property should allow the best possible approximation.

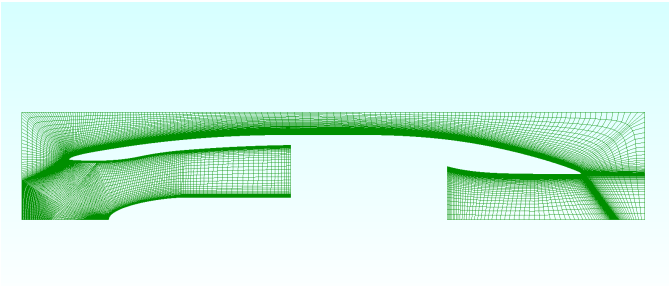

Figure 2.4: Bi-dimensional representation of the waterjet coarse structured mesh

2.5.3 Hull Mesh

The hull is represented in a three-dimensional quadrangular domain in which the entire flow field is analysed. The geometry is taken from the work developed at the Naval Surface Warfare Centre, Carderock Division, in West Bethesda, in which the model is chosen "to mimic the physics

and response to waves of a typical planing hull by using a modern planing hull bow shape and a prismatic hull aft of the bow area to minimize the geometric variables", [15].

Hull Mesh - Analysis

The process of grid refinement is computed starting from a coarse "original" mesh and it includes three different cases that need to be singularly analysed to discover possible sources for divergence.
The coarse mesh of the hull with 3219415 cells is refined with the following refinement factors "RF":

- $RF = 1.25$ leads to 3826502 cells that correspond to a coarse-medium mesh;
- $RF = 1.45$ leads to 5735675 cells that corresponds to the medium case;
- $RF = 2$ leads to 10150003 cells that corresponds to the fine grid.

In tables 2.1 the maximum and mean skewness values are reported to investigate cell distortion in every grid domain.

Domain	Maximum	Average
hull	0.87396457	0.076080743
air	0.81874704	0.022635425
inlet	0.37832655	0.031172517
channel side	0.34392638	0.022550664
outlet	0.37832655	0.031172517
seabed	0.53900521	0.036466335
symmetry	0.81773867	0.022762135

(a) COARSE mesh

Domain	Maximum	Average
hull	0.87397013	0.074296736
air	0.81877524	0.022319673
inlet	0.29028169	0.025652044
channel side	0,04018011	0.008919302
outlet	0.29028169	0.025652044
seabed	0.53890609	0.034050361
symmetry	0.81773823	0.022201446

(b) COARSE-MEDIUM mesh

Domain	Maximum	Average
hull	0.87398436	0.071423063
air	0.81826967	0.020526449
inlet	0.38683196	0.040457138
channel side	0.3440063	0.015330846
outlet	0.38683196	0.040457138
seabed	0.53944902	0.025668804
symmetry	0.8175608	0.020899579

(c) MEDIUM mesh

Domain	Maximum	Average
hull	0.87400564	0.05744408
air	0.8178303	0.019306396
inlet	0.3527045	0.01557352
channel side	0.34240959	0.012548086
outlet	0.3527045	0.01557352
seabed	0.5380458	0.019615546
symmetry	0.81733752	0.019959542

(d) FINE mesh

Table 2.1: Analysis of the maximum and mean skewness values for various mesh refinement factors.

Hull Mesh - Sensitivity

The previous cases, analysed in hull's mesh validation, are now considered to compute also the mesh sensitivity, which is carried out from the simulation of the isolated hull geometry.
The coarse, coarse-medium ($RF = 1.12$), medium ($RF = 1.45$) and fine ($RF = 2$) meshes are simulated in Ansys Fluent under the following boundary conditions:

- $p_{out} = 101325\ Pa$: the pressure outlet is considered uniform in the entire outlet domain and it equals the atmospheric pressure (the pressure increase given by Stevino's Law is neglected because of the shallow water);
- $V_{in} = 5.56\ m/s$: the velocity inlet is also constant all over the inlet domain.

Then, for salt see water, the following parameters are used:

- $\rho = 1025\ kg/m^3$: the water is an incompressible fluid so the density remain constant;
- $\mu = 0.001077\ kg/ms$: dynamic viscosity.

The numerics are set up using the "coupled" system for pressure and velocity equations, starting from a "first order upwind" discretization of pressure, momentum, kinetic energy and dissipation and then increasing them to the second and third order while increasing also the Courant Number.
This methodology allowed to reach a good convergence level as shown in Figure 2.5a, where the hull drag coefficient is reported for each different mesh.

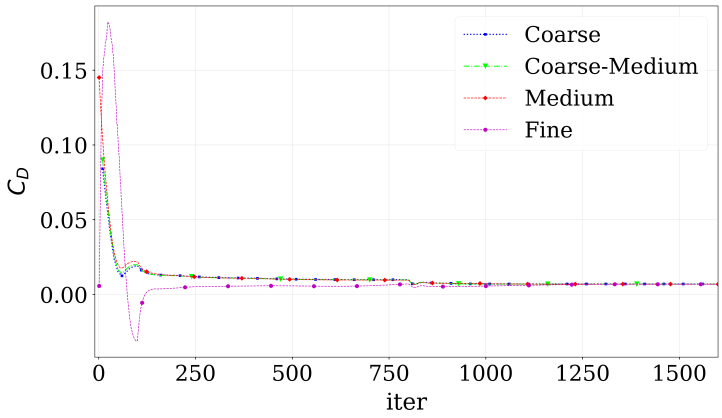

(a) Convergence of the drag coefficients

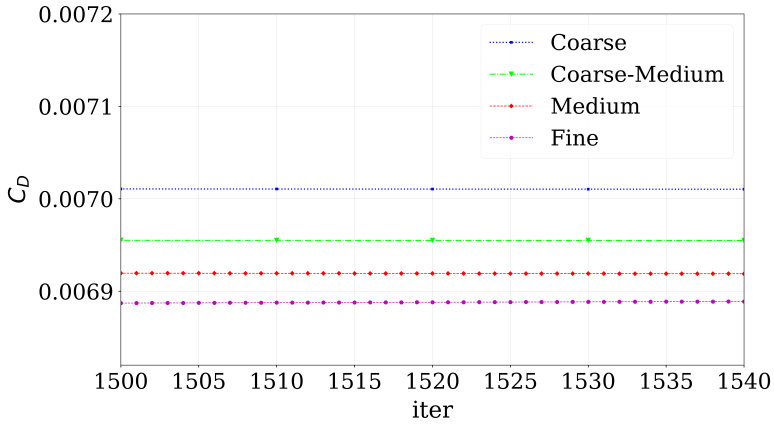

(b) Zoom on the convergence of drag coefficients

Figure 2.5: Convergence behaviour of the hull drag coefficients for the four different meshes with respect to the iteration number

Here it is possible to observe that the behaviours of the three coarser meshes are quite identical while the finest one has a slightly different trend, but they basically converge to the same value. In figure 2.5b a zoom on the converged part of the hull drag coefficients shows that these values have no oscillatory trend and are pretty much stable.
In a mesh sensitivity analysis it is important also to verify the convergence of a meaningful parameter to an asymptotic value (e.g. hull drag coefficient). This method leads to the evaluation of an approximate numerical solution that must be similar to that represented in Figure 2.3. In Table 2.2 the four meshes' drag coefficients are reported while in Figure 2.6 its convergence behaviour can be observed with increasing mesh resolution.

Mesh refinement	C_D
Coarse	0.11575502
Coarse-Medium	0.11486454
Medium	0.11421643
Fine	0.11394401

Table 2.2: Drag and drag coefficients of the hull speeding at $5.56\ m/s$

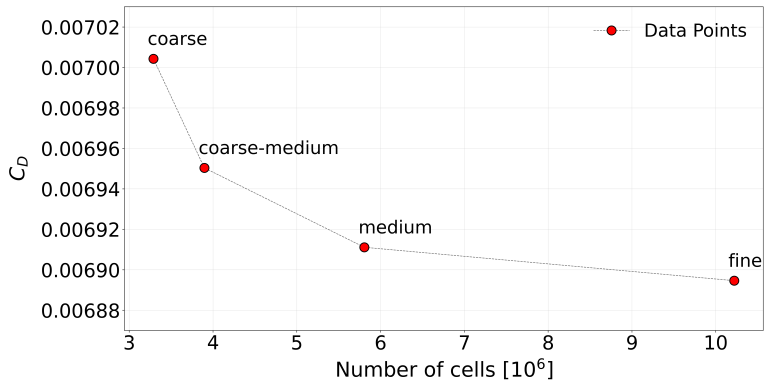

Figure 2.6: Drag coefficient convergence of the four different mesh resolutions

An other study carried out on this geometry is about the pressure coefficient on the hull's surface to implement a further validation of the four chosen meshes. Static pressure is computed along the keel and at the hull's most external line, at the boundary with the free surface. This line is chosen just to verify the different meshes in the "virtual domain" and not to obtain some physical characterising results because during the navigation the free surface is very variable). Once the static pressure is known it is very easy to calculate the pressure coefficient as:

$$C_p = \frac{p_{stat} - p_\infty}{\frac{1}{2}\rho {v_\infty}^2} \tag{2.20}$$

In the following images 2.7 and 2.8 the pressure coefficient computed on these two lines is reported for all the four mesh resolutions. It results clear that the data are quite super imposable and it is possible to affirm that the hull meshes are validated.

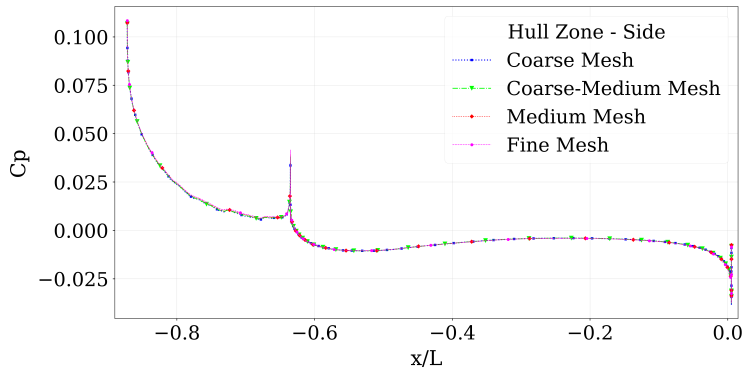

Figure 2.7: Pressure coefficients on the most external line of the hull

From the analysis of the trend shown in the graph, a sudden increase in the pressure coefficient leads to a small separation of the flow. It is caused by the positive pressure gradient generated by the change in curvature in the hull.

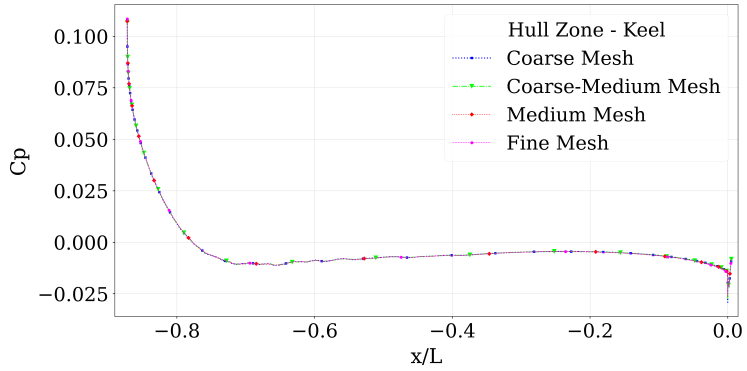

Figure 2.8: Pressure coefficients on the keel of the hull

2.5.4 Hull Installed ODW

In this paragraph, the hull installed Outboard Dynamic-inlet Waterjet is finally analysed. The complete geometry mesh generation is carried out using a script, which takes the individual meshes of the isolated three-dimensional hull and bi-dimensional propulsor and merges them into a single domain. The problem of the two different mesh dimensions is solved by setting up a revolution of the isolated ODW around its rotation axis.

Hull Installed ODW - Analysis

Before proceeding with the simulations, it is essential to perform an accurate mesh analysis on the geometry of the hull installed Outboard Dynamic-inlet Waterjet case. This process is critical, as the coupling of two geometries that have been studied and meshed separately may result in a discretisation with a high number of highly distorted cells, which can cause significant convergence difficulties.
The first analysis is carried out by merging the meshes of the individual components with different refinement factors. Specifically, the following cases are considered:

- hull-coarse and jet-coarse: this results in the coarsest mesh, which contains a total of 15512813 cells;
- hull with $RF = 1.45$ and jet-medium: this configuration contains 24618769 cells;
- hull-fine and jet-fine: the total number of cells is 39303653.

In this analysis, the parameter under consideration is still the skewness, which is reported in Table 2.3 for the different surfaces of the geometry as a function of the grid refinement. The aim is to identify the most critical regions and, if necessary, to make adjustments to improve the mesh. The data presented below highlight specific domains where a certain number of cells exhibit potentially problematic skewness. Therefore, particular attention should be paid to these areas, even though the average values are very good, suggesting that the number of highly distorted cells is extremely low.

Domains	Maximum	Average
hull	0.87396457	0.076080743
air	0.81000932	0.023201874
inlet	0.37832655	0.031172517
channel side	0.34392638	0.022550664
outlet	0.37832655	0.031172517
seabed	0.53900521	0.036466335
symmetry	0.94376435	0.069944525
mass-flow-inlet	0.91560821	0.037576546
exhaust	0.89223616	0.056521598
jet-inside	0.0099240721	0.0018296633
jet-outside	0.0099999801	0.0038610787
spinner	0.97000276	0.012411999

(a) COARSE mesh

Domains	Maximum	Average
hull	0.79830026	0.020706771
air	0.82094717	0.021400776
inlet	0.38683196	0.040457138
channel side	0.3440063	0.015330846
outlet	0.38683196	0.040457138
seabed	0.53944902	0.025668804
symmetry	0.92734083	0.053905225
mass-flow-inlet	0.038806825	0.037576546
exhaust	0.95151351	0.059432046
jet-inside	0.0099999873	0.0017707149
jet-outside	0.0099997828	0.00313413
spinner	0.97000039	0.0067615348

(b) MEDIUM mesh

Domains	Maximum	Average
hull	0.79833267	0.014658602
air	0.8241705	0.019635063
inlet	0.3527045	0.01557352
channel side	0.34240959	0.012548086
outlet	0.3527045	0.01557352
seabed	0.5380458	0.019615546
symmetry	0.94223844	0.049431119
mass-flow-inlet	0.89534129	0.050062312
exhaust	0.96703452	0.10218587
jet-inside	0.0099999873	0.0020436183
jet-outside	0.0099998917	0.0026832725
spinner	0.97000123	0.0051931239

(c) FINE mesh

Table 2.3: Surfaces skewness analysis for the coarse, medium and fine mesh of the hull installed ODW

The reported data show a general deterioration in skewness parameters compared to the isolated hull case, a behaviour that can be justified by the coupling of two different geometries.
By analysing in greater detail where the most distorted cells develop, several hotspots can be identified. In the coarse case, for example, there is a series of highly distorted cells within the fluid passage created between the hull and the waterjet. This distortion arises from the difficulty in connecting the meshes of the hull and propulsor, which have significantly larger and different cell sizes (Figure 2.9a). As the mesh is refined and the cell size is gradually reduced, the problem is gradually resolved and this is evident when examining the skewness values in the critical region, as shown in Figures 2.9b and 2.9c. The skewness decreases from 0.9437 in the coarse case to 0.8574 in the medium case, and finally to 0.7394 in the fine case. This trend can be demonstrated by the reduction of high-coloured cells in the figures.

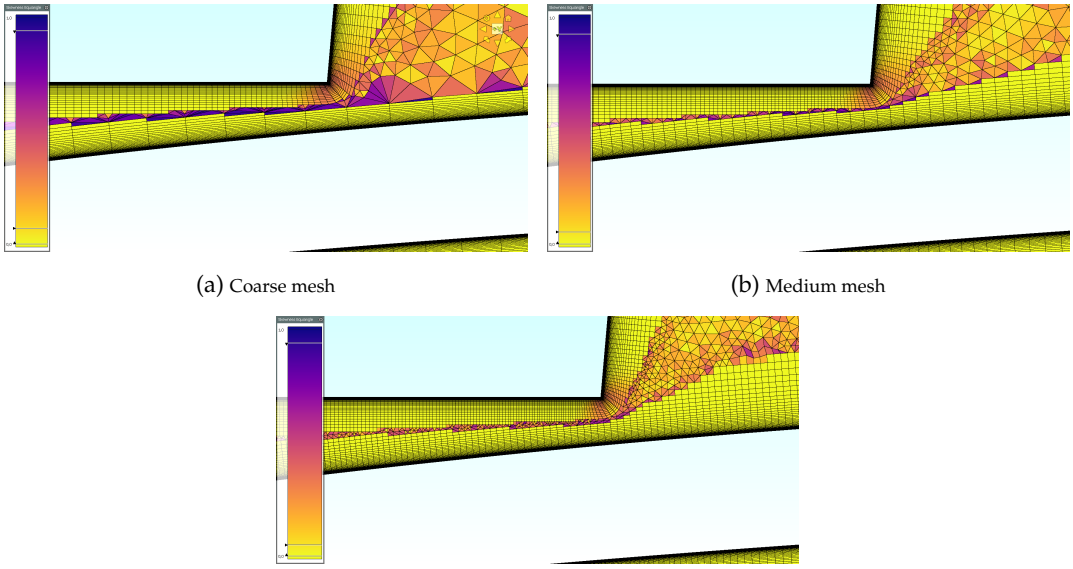

(a) Coarse mesh

(b) Medium mesh

(c) Fine mesh

Figure 2.9: Skewness representation in the critical zone between the hull and the ODW

A further investigation is conducted on the entire fluid domain, to identify regions of high-distortion cells that could compromise the convergence of the simulations. This analysis leads to the results presented in Table 2.4 that reveal a non-negligible number of cells with high skewness.

Configuration	**Mean Skewness**	$\mathbf{N_{cells} > 0.9}$	$\mathbf{\%_{cells} > 0.9}$
coarse	0.28210212	148589	0.958%
medium	0.23781247	345306	1.4%
fine	0.22181959	964144	2.45%

Table 2.4: Water domain skewness analysis for the coarse, medium and fine hull installed jet meshes.

By analysing the cell distortion through the application of filters in the meshing software, it is possible to identify the most critical areas: the leading edge of the inlet and the trailing edge of the nozzle. These regions exhibit the highest distortion levels, resulting in the lowest cell quality across the entire computational domain. Consequently, the values computed in these cells can cause the simulation to diverge or give results that are likely to be unreliable or significantly affected by numerical errors, potentially compromising not only local flow properties, but also the overall downstream solution. As shown in 3, this is also a very critical zone, where cavitation can occur, causing further complications of fluid flow.
Moreover, as evidenced by the reported data, mesh refinement does not substantially mitigate this issue; instead, it increases the percentage of cells with critical distortion. This suggests that the problem does not originate from insufficient grid resolution but from improper handling of the solver at the interface between the domain and the ODW's boundary layer.
For this reason, modifications were implemented both on the propulsor mesh and within the script responsible for geometry merging and mesh generation. These adjustments effectively resolved the issues by significantly reducing the number of highly distorted cells. The improvement is clearly demonstrated in Figure 2.10 and Table 2.5, where a comparison between the initial and modified meshes highlights the necessary refinements required for the accurate execution of the simulations. In Figure 2.10a the old configuration ODW is reported with a filter that highlights the cells with skewness greater than 0.9, so only the very distorted cells can raise some convergence problems. As evidenced before, the highlight of the inlet and the trailing edge of the nozzle has a thick black and orange layer of low-quality cells that disappear in the second image 2.10b

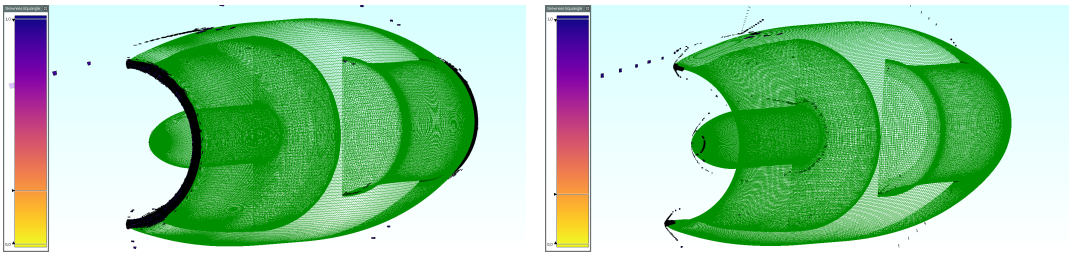

(a) OLD hull installed ODW mesh

(b) NEW hull installed ODW mesh

Figure 2.10: Comparison between the old and the new hull installed ODW mesh skewness at the inlet leading edge

Configuration	**Mean Skewness**	$\mathbf{N_{cells} > 0.9}$	$\mathbf{\%_{cells} > 0.9}$
Medium OLD	0.23781247	345306	1.4%
Medium NEW	0.22109763	36636	0.138%

Table 2.5: Comparison between the old and the new mesh skewness

Based on the results obtained from the grid convergence study conducted on the three-dimensional

hull and the hull installed ODW, the medium resolution hull mesh with a refinement factor of 1.45 and the new adapted waterjet grid are chosen as baseline for a new script, responsible for generation of the installed case.

2.6 ODW - Installation

The main focus of this thesis is on analysing the effects of the Ouboard Dynamic-inlet Waterjet's installation position on the hull and specifically examining the interaction phenomena between the two components. To conduct this study, many simulations must be performed in various installation position to find the best possible theoretical configuration.

2.6.1 Baseline configuration

To perform the aforementioned analysis, it is necessary first to define a baseline geometry and corresponding reference points that allow the characterisation of the various configurations. The trailing edge of the keel is designated as the origin of the coordinate system, serving as the zero point from which the distances to the leading edge of the upper lip of the inlet are measured. This reference system is illustrated in Figure 2.11, where Δx and Δz denote, respectively, the horizontal and vertical distances of the propulsor's leading edge relative to the defined origin.

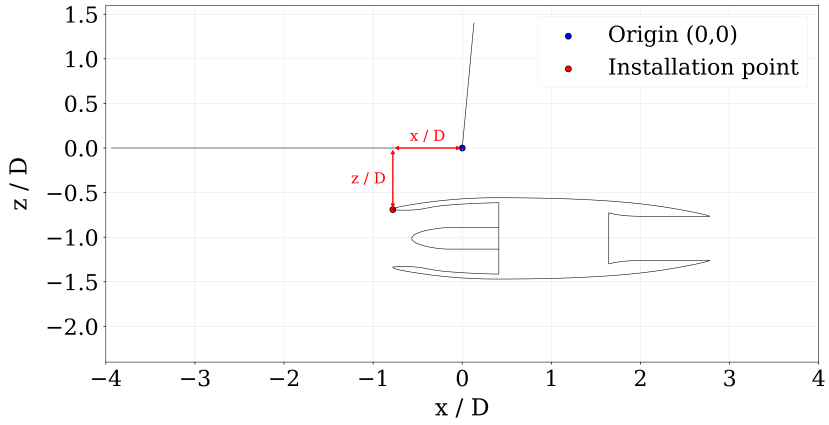

Figure 2.11: Caption

2.6.2 Installation positions

This section defines all the simulated points in which the ODW is installed on the hull for the simulations. As previously stated, the fundamental objective is to determine the optimal theoretical installation position that ideally satisfies all the key requirements, like minimum hull and jet drag and maximum available net thrust. To identify the most favourable installation

region of the propulsor, a matrix grid of installation points must be considered, simulated, and then analysed. The following Figure 2.12 illustrates all the positions assumed by the leading edge of the upper lip of the intake in the different cases. The coordinates are referred to the trailing edge of the hull keel $(0, 0)$ and normalised with respect to the pump inlet diameter D. The more forward installation sections are represented by only two points because the standard upper positions cause the ODW to overlap the hull's keel, and therefore an intermediate position with vertical coordinate is considered $z/D = -0.2969$

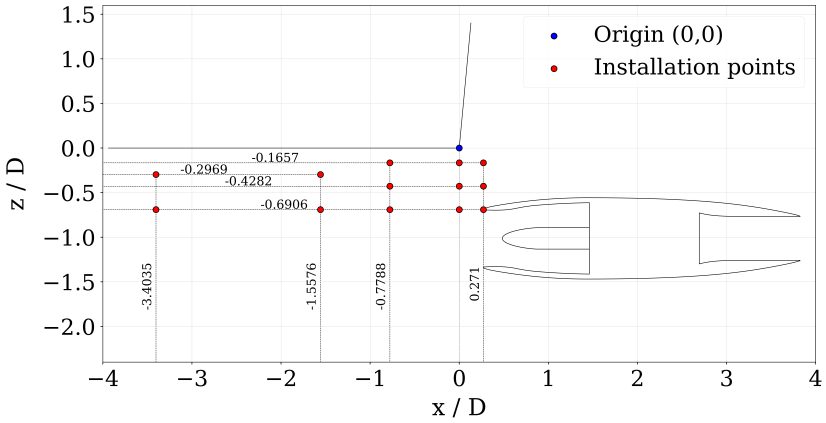

Figure 2.12: Grid of points in which the upper inlet lip is positioned with respect to the hull

To avoid potential issues such as simulation divergence, Table 2.6 presents key grid metrics, including the average skewness value, the number of highly distorted cells with a skewness exceeding 0.9, and the corresponding percentage relative to the total number of cells. These values are reported for all mesh configurations considered in this study.
For a better understanding, the non-dimensional coordinate referred to the installation positions are identified with the following convention: $x/D = \tilde{x}$ and $z/D = \tilde{z}$, which lasts for the entire thesis.

$\tilde{\mathbf{x}}$; $\tilde{\mathbf{z}}$	**Mean Skewness**	$\mathbf{N_{cells} > 0.9}$	$\%_{\mathbf{cells}} > \mathbf{0.9}$
0.271 ; -0.1657	0.22138331	36167	0.136%
0.271 ; -0.4282	0.22191916	36140	0.135%
0.271 ; -0.6906	0.22225662	36604	0.136%
0 ; -0.1657	0.22127078	36472	0.137%
0 ; -0.4282	0.22213088	36120	0.135%
0 ; -0.6906	0.22224684	36454	0.136%
-0.7788 ; -0.16576	0.22109763	36636	0.138%
-0.7788 ; -0.1657	0.22184425	36204	0.135%
-0.7788 ; -0.6906	0.22229106	36358	0.135%
-1.5576 ; -0.2969	0.22118802	36529	0.137%
-1.5576 ; -0.6906	0.22248264	36591	0.136%
-3.4035 ; -0.2969	0.22169474	35935	0.135%
-3.4035 ; -0.6906	0.22274712	35793	0.133%

Table 2.6: Skewness analysis on different installation position.

3 RESULTS

The main contribution of this thesis consists in the analysis of the Outboard Dynamic-inlet Waterjet installation positions to investigate the installation effects in line with the aeronautically inspired nature of this propulsive system. Installation effects are well-known issues in the aerospace field, as they can lead to undesired impacts on the performance of the propulsion system. Many analyses have shown that the performance recorded for an engine installed on the wing differs from that obtained simply by summing the individual effects of the two components. Therefore, performance evaluation is particularly significant when simulating the entire geometry after installation.
Most of the analyses and data processing are performed using Ansys Fluent, which plays a key role in obtaining the results presented in this chapter.

3.1 Results validation

3.1.1 Convergence

As described in Section 2.1.3, the first necessary (but not sufficient) criterion to determine the success of a simulation is to analyse the residual trends, ensuring that they approach zero with increasing number of iterations, and to verify the convergence of the monitored parameters to a finite value. Recalling that residuals are defined as the difference between the solution in iterations i and $i-1$, it is possible to examine the residuals of the system's governing equations, which are automatically generated by Fluent.
These standard reference equations include: continuity, x-velocity (u), y-velocity (v), z-velocity (w), turbulent kinetic energy (k) and specific dissipation rate (ω). In addition to these, four other terms need to be considered: two of them are related to the monitoring drag force on the hull and the total drag coefficient of the propulsor, both of which must converge to a finite value, and two further terms represent the residuals of these monitored quantities, which should instead tend to zero. A common practice is to define convergence as achieved when all residuals reach values of the order 10^{-6} or lower.
In Figure 3.1 the typical residual behaviours of the governing equations are reported.

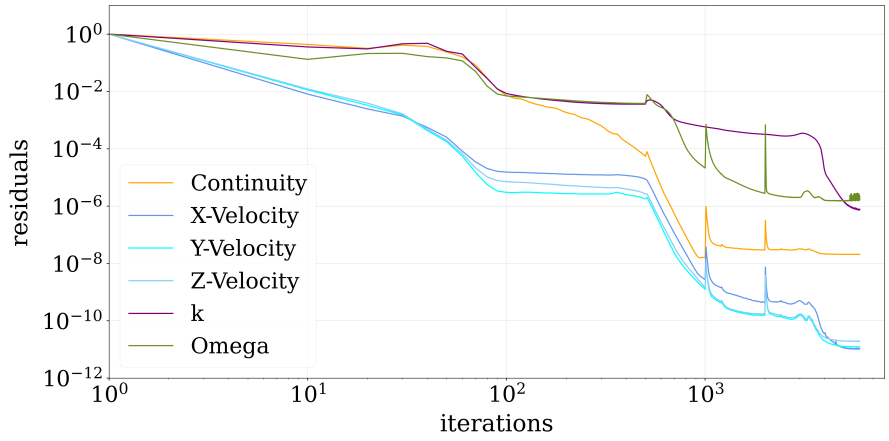

Figure 3.1: Standard behaviour of the residuals with respect to the number of iterations

This logarithmic scale graph refers to the simulation under design conditions, with the propulsor installed at position $(0\ ;\ -0.4282)$. A very satisfactory level of convergence is obtained, with maximum residuals for the dissipation equation reaching $2 \cdot 10^{-6}$.
From the residuals trend, it is also possible to identify the points at which the spatial discretisation order is increased in the pressure, momentum, energy, and dissipation equations. These transitions are characterised by a sudden peak in the residual trends, but the values quickly return to their previous levels after a few iterations.
To complement the converge analysis, Figure 3.2 presents the convergence of the drag values of the hull, made dimensionless using the design velocity and the hull reference area, as well as the drag coefficient of the propulsor, calculated as the contribution of all its constituent surfaces. The trend is similar to that shown in Figure 2.5a, with initial sharp fluctuations in C_D that eventually stabilise and rapidly converge to their final value.
In line with the analyses conducted on the hull, Figures 3.2b and 3.2c illustrate the values of the drag coefficients from iteration 5700 to 6000, providing further evidence of convergence and demonstrating the absence of oscillations in the result, which is indicative of a solid stable solution.

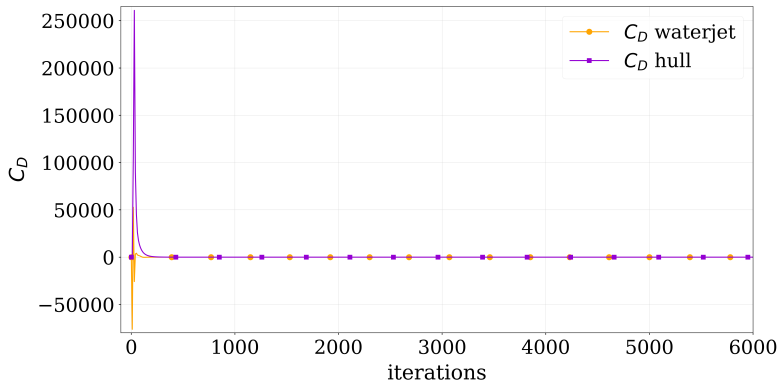

(a) Drag coefficient convergences

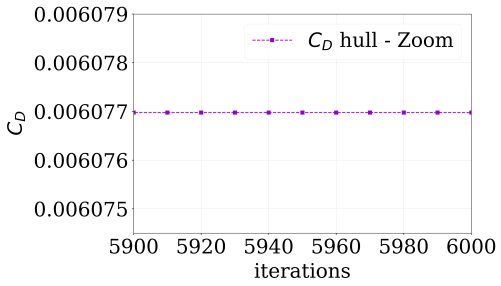

(b) Convergence of the hull drag coefficient

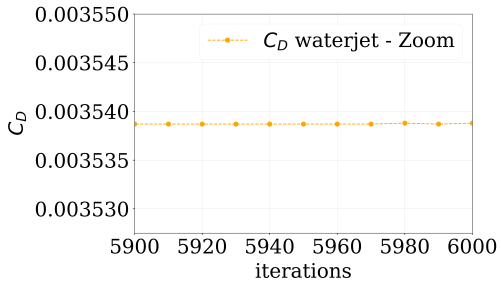

(c) Convergence of the ODW drag coefficient

Figure 3.2: Convergence behaviour of the hull and waterjet drag coefficients with respect to the increasing number of iterations

3.1.2 Boundary Layer resolution

Another fundamental aspect that must be faced to assess the precision and reliability of the simulation results is the analysis of the wall parameter y^+, introduced in Section 2.1.2 and specifically defined in equation 2.2.
The boundary layer developing along the surfaces of bodies immersed in a viscous fluid can play a crucial role in the fluid motion, altering both the flow characteristics and the performances. This is the reason why, in simulations requiring a high level of reliability, it is essential that the boundary layer be resolved rather than modelled numerically. The parameter y^+ determines whether the near-wall flow is resolved or approximated by the software and, as such, is of critical importance.
The objective is to ensure that the boundary layer is fully resolved on all surfaces exposed to the fluid flow, which means that the value of wall y^+ remains below 1. The following figures represent this value behaviour for different selected hull sections 3.3 and for all the walls of the propulsion system 3.4.

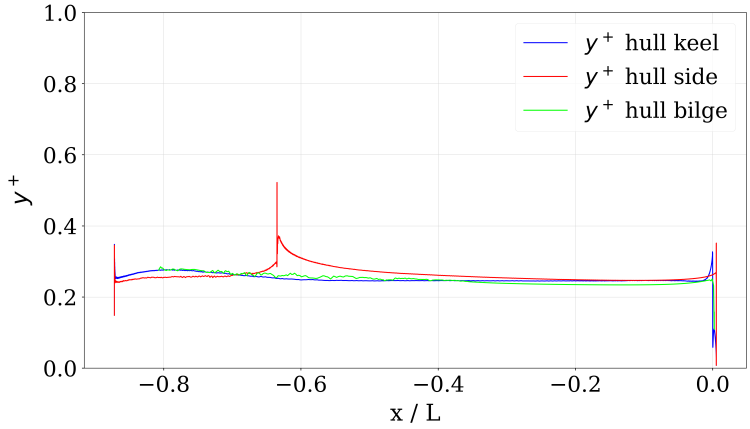

Figure 3.3: y^+ behaviour in different sections of the hull

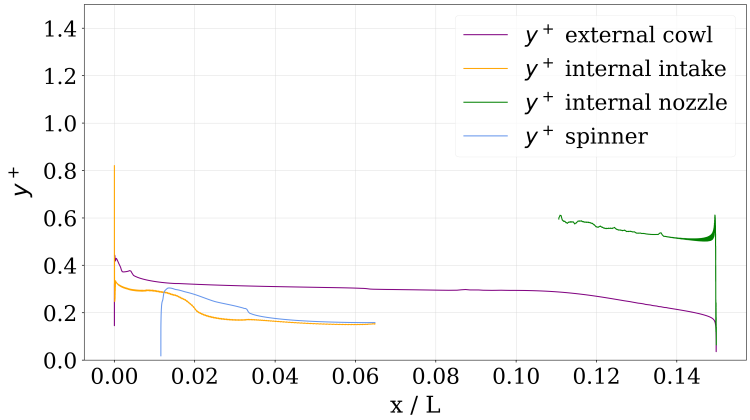

Figure 3.4: y^+ behaviour in different sections of the ODW

In both the reported images, the y^+ values are below the critical threshold of 1 of a good margin for most of the surfaces. This suggests, with reasonable confidence, that the boundary layer is consistently resolved rather than modelled.
Regarding the propulsor, it should be noted that the 3D geometry is generated by revolving the 2D profile around the rotation axis. As a result, the structured mesh remains uniform along the entire circumference, allowing single-section analyses.
The hull instead is not built like a solid of revolution, so every section should be singularly analysed. However, by evaluating the safety margins of the obtained y^+ values across the three examined regions (the keel, the surface in contact with the waterline, and a section along the hull bilge located 75 cm below the surface), it can reasonably be concluded that the entire boundary layer is properly resolved.

3.2 Installation effects

Since the ODW is a marine propulsion system inspired by aeronautic technology, installation effects are also relevant in the naval field. The presence of the waterjet induces flow variations due to the interactions that arise between the propulsor and the hull. This phenomenon is demonstrated in Table 3.1, where the hydrodynamic drag of the hull in the isolated and installed cases is reported at a coordinate of $(0\ ;\ -0.4282)$ while travelling at cruise and "*hump*" speeds, respectively.

Configuration	$\mathbf{C_D}_{\mathbf{hull}}^{\text{design}}$	$\mathbf{C_D}_{\mathbf{hull}}^{\text{off-design}}$
Isolated hull	0.01331919	0.01361237
Hull installed jet	0.0121541	0.01186373

Table 3.1: ODW installation effects on the hull drag for design and off-design conditions

It is therefore evident that the engine installation affects the hull drag (in this case, in a beneficial way), clearly demonstrating the mutual influence between the two bodies. This validates the theory of installation effects even in the case of a marine propulsion system.

3.3 Pressure Field

In this section the pressure field is analysed. The pressure directly influences the hydrodynamic forces acting on a body submerged in a fluid, and it reveals key information about the flow behaviour.

3.3.1 Cavitation research

One of the most critical aspects of incompressible flows involving liquids such as water is the identification of cavitation formation. The potentially catastrophic effects of this phenomenon have already been discussed in the dedicated Section 2.4, while the following paragraph aims to assess both the probability of cavitation occurring and the regions where cavitation bubbles may form.
Recalling that cavitation occurs in regions where the local fluid pressure drops below its vapour pressure - approximately $2300\ Pa$ for water at $20°C$ - in Table 3.2 the values of the minimum pressure coefficient are reported across the flow field for the design and off-design conditions, with the aim of identifying areas where this critical limit may be exceeded. By applying Equation 2.20 with the vapour pressure, the critical pressure coefficients C_p^* are computed under design and off-design conditions, and reported in the following table.

Configuration	$\mathbf{C_{p\ min}}^{\text{design}}$	$\mathbf{C_{p\ min}}^{\text{off-design}}$
Critical value	-0.754763	-3.943255
$0.271\ ;\ -0.1657$	-0.50215726	-5.21257473
$0.271\ ;\ -0.4282$	-0.53476267	-5.03279789
$0.271\ ;\ -0.6906$	-0.4663156	-5.03277161
$0\ ;\ -0.1657$	-0.67179333	-5.17809891
$0\ ;\ -0.4282$	-0.53311064	-4.9983065
$0\ ;\ -0.6906$	-0.46587686	-5.03856354
$-0.7788\ ;\ -0.16576$	-0.95097486	-4.86436854
$-0.7788\ ;\ -0.4282$	-0.53299159	-4.87031172
$-0.7788\ ;\ -0.6906$	-0.46270171	-4.91150873
$1.5576\ ;\ -0.2969$	-0.54334945	-4.87534781
$1.5576\ ;\ -0.6906$	-0.44158968	-4.88659982
$-3.4035\ ;\ -0.2969$	-0.52924537	-4.85961915
$-3.4035\ ;\ -0.6906$	-0.42924256	-4.88659982

Table 3.2: Minimum pressure coefficient value in the entire fluid domain.

The results obtained under the design conditions show that only one installation point leads to the formation of a low-pressure region, where the pressure coefficient drops below the critical value. This point, located at coordinates $(-0.7788\ ;\ -0.16576)$, corresponds to the configuration in which the external cowl of the engine is positioned closest to the keel of the hull.
By analysing the pressure field on the symmetry plane it is particularly interesting to note that cavitation occurs in two different zones: there is a cavitation principle at the upper inlet leading edge and a larger cavitation zone at the upper nozzle outlet. In the first position, the pressure drops below the vapour tension in a really small point, while at the nozzle exit the low-pressure zone is bigger with a higher negative pressure, leading to a more intense cavitation. In Figure 3.6 by removing the external wall of the nozzle, it is possible to clearly observe the dark blue low-pressure zone on the upper lip of the nozzle exit, with a pressure coefficient $C_p < C_p^*$.

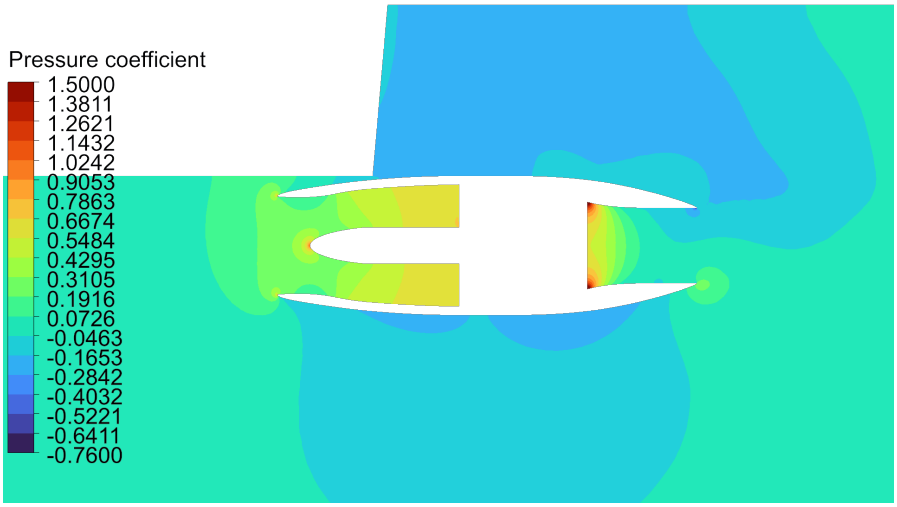

Figure 3.5: Pressure coefficient contour on the symmetry plane under design condition, with installation coordinates $(-0.7788\ ;\ -0.16576)$.

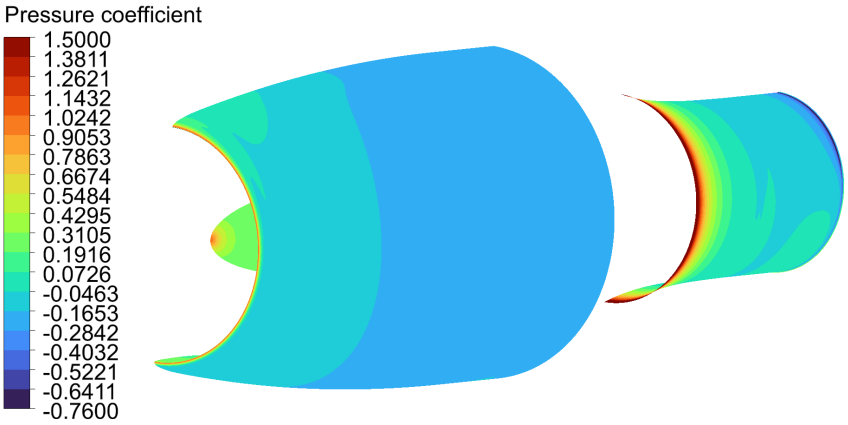

Figure 3.6: Pressure coefficient contour on the 3D ODW model under design condition, with installation coordinates $(-0.7788\ ;\ -0.16576)$.

In Figure 3.5 it is possible to analyse the pressure field of the fluid domain. Behind the hull the turbulent wake creates a low pressure zone. At the inlet it is possible to observe an increasing pressure before the highlight; this is due to the pre-compression caused by the divergent shape of the streamtube under the design condition with an $IVR = 0.85$. A low pressure zone is also visible under the propulsor, where the flow is accelerated.

To demonstrate the mentioned pressure drops at the intake (Fig.3.7a) and at the nozzle (Fig. 3.7b),

the following Figure 3.7 represents the C_p in the symmetry plane, with respect to the normalised axial coordinate (Equation 3.1), respectively compared to the results of the lower installation position $(-0.7788\ ;\ -0.4282)$. To better understand, the limit of the critical design pressure coefficient is also reported, $C^*_{p\ \text{design}}$

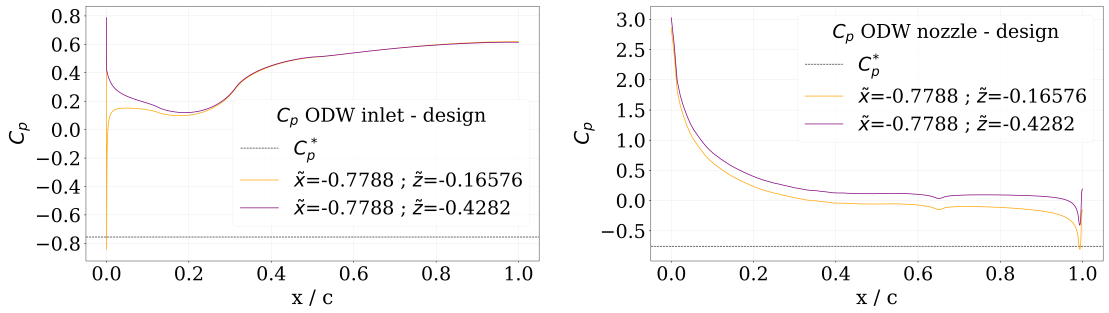

(a) C_p Inlet

(b) C_p Nozzle

Figure 3.7: Pressure coefficients behaviour at the inlet and at the nozzle of the ODW, installed in two different positions to demonstrate cavitation insurgence under design condition only for the $(-0.7788\ ;\ -0.16576)$ case.

In the first image 3.7a it is very clear the different behaviour of the pressure coefficients at the highlight of the inlet. For the installation point with coordinate $(-0.7788\ ;\ -0.16576)$, C_p overcomes the critical pressure coefficient, incurring the risk of cavitation phenomena. The second image shows more similar trends between the two configurations, but the inlet of the nearest installation point is subjected to cavitation too.
From the analysis of the reported figures it is also possible to extract the extension of the cavitation zone. The critical pressure coefficient is overcome in a very short interval at the inlet highlight, while at the nozzle exit the under-pressure zone is slightly bigger.

In off-design conditions, as reported in the second column of Table 3.2, cavitation occurs regardless of the installation position, making the hump point particularly critical. Figure 3.8 shows the location on the symmetry plane at which the minimum pressure is reached. The cavitating region corresponds to the internal inlet lip, where the contours assume a dark blue colour. At low speeds, the free-streamtube has a cross-sectional area larger than that of the propulsor's highlight, effectively acting as a converging duct.
The shape of the streamtube can be proven by the presence of a lower pressure zone before the inlet highlight, where the streamtube converges. It is also possible to carefully compare the pressure coefficient contours of the design and off-design conditions and observe that the stagnation point, characterised by a small brighter zone, moves toward the external lip zone from Figure 3.5 to Figure 3.8.
As a result, the external flow does not reach the engine inlet in a straight path but is forced to bend around the inlet leading edge. To make this happen, a negative pressure gradient must

form in this region, which may locally drop below the vapour pressure. This mechanism can lead to the formation of cavitation bubbles in areas where the pressure coefficients fall below their critical values.

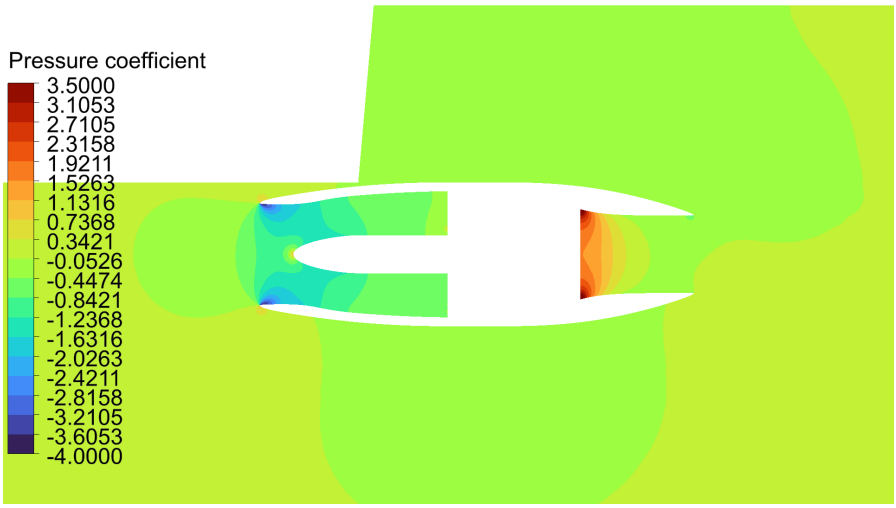

Figure 3.8: Pressure coefficient contour on the symmetry plane under off-design condition, with installation coordinates $(-0.7788\ ;\ -0.16576)$.

A further demonstration of the presence of cavitation in all off-design configurations is now reported in Figure 3.9, where the intake pressure coefficient of five sample installation points is reported.

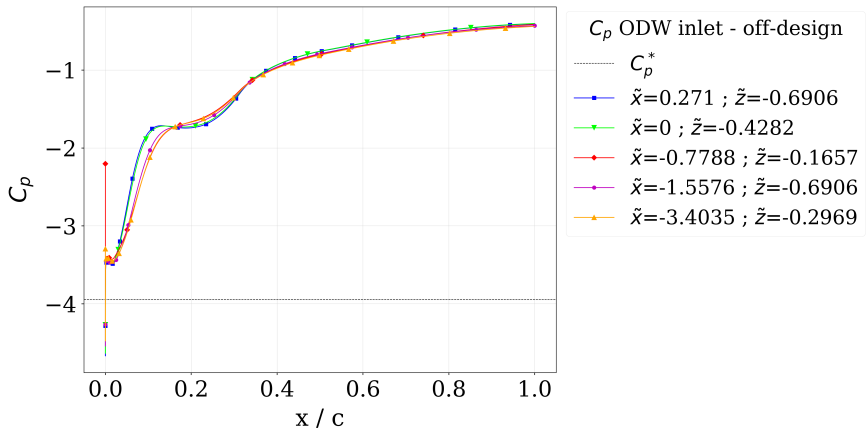

Figure 3.9: Pressure coefficient at the inlet for five different ODW installation position

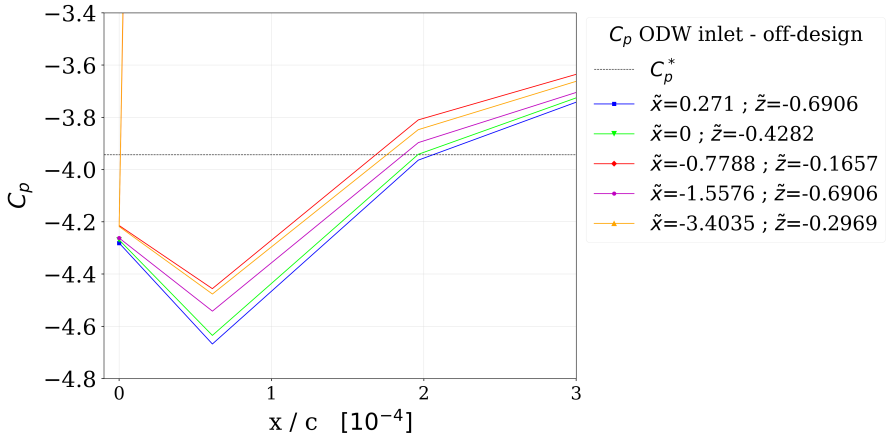

Figure 3.10: Zoom to display the negative pressure coefficient at the inlet highlight for five different ODW installation position

In the images also the critical pressure coefficient is represented, C_p^*, showing the limit under which cavitation phenomena occur under off-design conditions. From this analysis, it is clear that each installation position is affected by the potential formation of cavitation bubbles that can cause the problems discussed in Section 2.4. This is the reason why, in the following paragraphs of the thesis, the off-design conditions are highlighted to evidence the risk of cavitation phenomena. To complete the cavitation analysis, Table 3.3 reports the areas involved in cavitation phenomena for each installation point under critical off-design conditions. This parameter is computed in CFD-Post by calculating the area of the internal and external intake in which the pressure is below the vapour pressure. The values obtained are then made non-dimensional by the division for the pump face inlet area, getting the area coefficient: $\tilde{A} = A_{cav}/A_{pump}$, which denotes the percentage of inlet subjected to cavitation with respect to the reference area.

Configuration	$\tilde{A}$
0.271 ; -0.1657	0.0008691
0.271 ; -0.4282	0.00087552
0.271 ; -0.6906	0.00087829
0 ; -0.1657	0.00087457
0 ; -0.4282	0.00087932
0 ; -0.6906	0.00088057
-0.7788 ; -0.16576	0.00089346
-0.7788 ; -0.4282	0.00089266
-0.7788 ; -0.6906	0.00088989
1.5576 ; -0.2969	0.00089615
1.5576 ; -0.6906	0.00089548
-3.4035 ; -0.2969	0.00089576
-3.4035 ; -0.6906	0.00089562

Table 3.3: Fraction of area subjected to cavitation phenomena.

From the results obtained, it is possible to observe a decreasing trend in the cavitation area coefficient as the longitudinal installation position shifts towards the stern. This indicates a reduction in the area affected by cavitation and, consequently, a slight mitigation of the phenomenon.

3.3.2 Keel - Pressure distribution

In this section, the pressure coefficients that develop on the outer surfaces of the hull and propulsor are analysed under both design and off-design conditions. The aim is to assess the effects of the mutual interaction between the hull and the propulsion system, depending on the position of the propulsor installation.
The analysis considers two extreme configurations: on one hand, positions in which the propulsor is installed closer to the hull along the vertical direction that are identified in the graphs with the name *"up"*; on the other hand, positions where the propulsor is located farther away, with a common vertical coordinate of $\tilde{z} = -0.6906$, identified with the name *"down"*. This approach allows for a clear identification of how longitudinal positioning affects the pressure field and how this influence changes with vertical distance from the hull.
The results are presented in the form of a non-dimensional pressure coefficient, calculated using Equation 2.20, and scaled by the reference velocities. The axial coordinate is also made non-dimensional to enable consistent comparisons across the different cases. Specifically, in the analysis concerning the hull, the coordinate is scaled with respect to the total length of the hull. In the next two images, the pressure coefficients computed along the hull's keel are reported; this area represents, in fact, the region most affected by the presence of the ODW. The results refer to the design condition for each longitudinal installation coordinate. By comparing the two images, it is also possible to assess how the pressure field varies with changing vertical position.

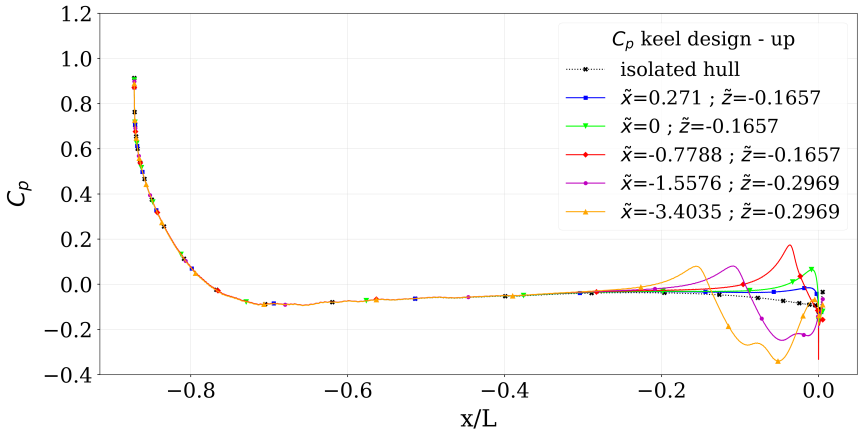

Figure 3.11: Pressure coefficient variation on the keel for varying longitudinal installation locations at vertical coordinate $z/D \geq -0.2969$, with an $IVR = 0.85$

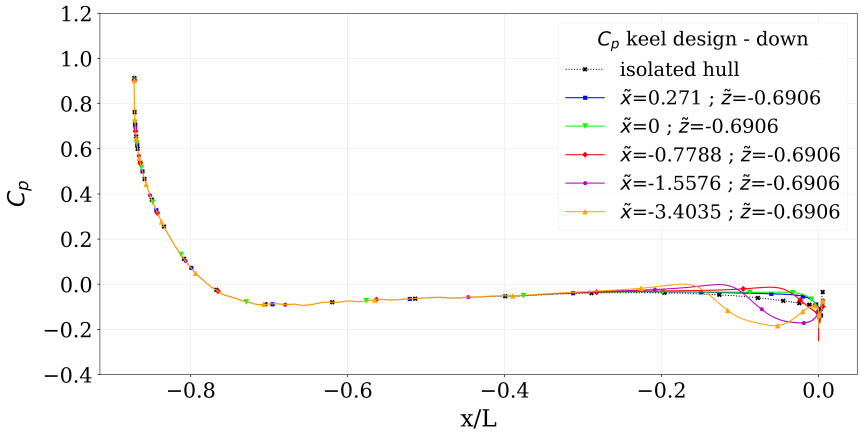

Figure 3.12: Pressure coefficient variation on the keel for varying longitudinal installation locations at vertical coordinate $z/D = -0.6906$, with an $IVR = 0.85$

The trend of the pressure coefficient can be divided into three distinct regions. The first one, located towards the stern, corresponds to the stagnation point of the flow and is thus characterised by a high pressure that rapidly decreases, becoming negative along the longitudinal direction of the hull, acting like a reversed airfoil. The second region is defined by a negative pressure coefficient ($C_p < 0$) with a very stable trend, where the flow moves undisturbed along the keel at a pressure lower than atmospheric, corresponding to a velocity higher than the reference cruise. The third region is instead characterised by fluctuations in the pressure coefficients, due to the presence of the propulsor. As can be seen by comparing the two plots, a propulsor installation position closer to the hull causes more significant disturbances in the flow.
In Figure 3.11, a substantial variation in the pressure coefficient can be observed. For installation

positions located below the hull ($x/D < 0$), there is an initial sharp increase, followed by a rapid decrease below the reference pressure value, represented by the black curve corresponding to the isolated hull case. The decrease in C_p corresponds to an increase in velocity, due to the formation of a sort of Venturi channel between the external wall of the propulsive system and the hull. Once the "channel" convergent section is passed, where the maximum velocity is reached, the pressure tends to rise to the reference value as the section begins to widen towards the nozzle area.
The first increase in pressure can be attributed to the shape of the streamtube under design conditions: the inlet area of the free streamtube will be smaller than the highlight area - $IVR < 0$ - thus forming a divergent conduit at the inlet of the intake. Following this trend, the flow around the streamtube is disturbed, leading to a possible thinning of the velocity profile inside the boundary layer of the hull's keel.
It is also interesting to note that the high positive pressure gradient, occurring in the red line and denoting a greater disturbance in the fluid flow, refers to the installation position in which the cavitation takes place even under design conditions. This is also the geometry in which there is the least clearance between the trailing edge of the hull and the external cowl of the propulsor, so the Venturi effect is maximised.
In Figure 3.12 a similar behaviour is represented, but the pressure gradient is much less pronounced. The initial adverse pressure gradient is absent, meaning that no disturbance is present and the peaks of the negative pressure coefficient are lower. This is due to a larger "channel" section that reduces the effects of the aforementioned phenomenon.

In the next Figures 3.13 and 3.14 instead, the off-design results are reported.

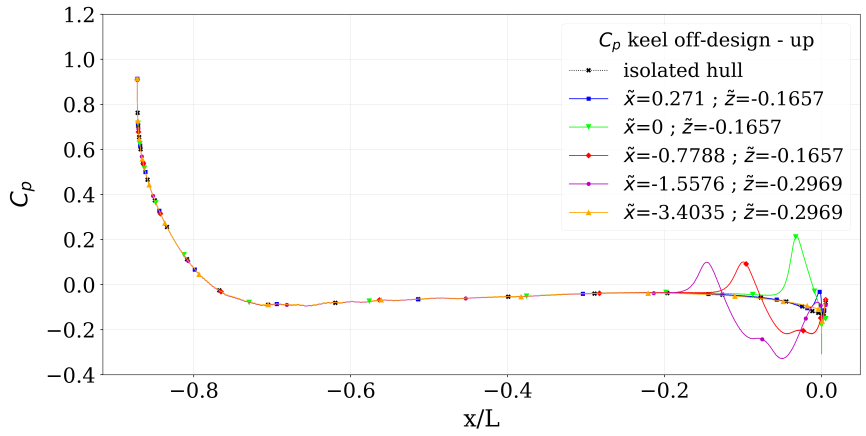

Figure 3.13: Pressure coefficient variation on the keel for varying longitudinal installation locations at vertical coordinate $z/D \geq -0.2969$, with an 1.425

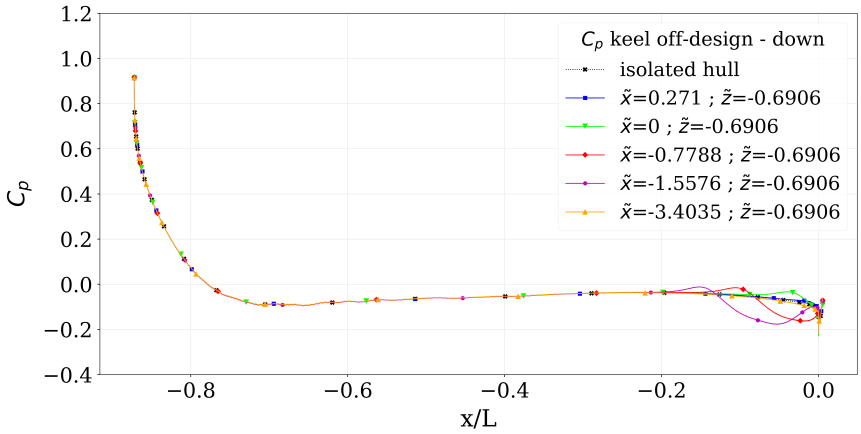

Figure 3.14: Pressure coefficient variation on the keel for varying longitudinal installation locations at vertical coordinate $z/D = -0.6906$, with an $IVR = 1.425$

By comparing the two images with those of the design case, a marked similarity can be observed, with closely matching trends in the two different configurations; there are, however, some differences.
The first concerns the intensity of the increase in the initial pressure coefficient, which compared to the one noticeable in Figure 3.11, it is quite higher, especially for the longitudinal position with coordinate $x/D = 0$. This behaviour is likely influenced by the presence of cavitation at the leading edge, which leads to separation and hydrodynamic deterioration of the flow passing through between the keel and the propulsor. In fact, this effect is much smaller in Figure 3.14.
The second difference lies in the position of the C_p peaks, which, in the design cases, are located further behind, near the stern of the boat, while in this condition they are closer to the installation position. This is due to the flux velocity, for which the perturbation travels slower and reaches zones nearer to the inlet highlight.
The third and final difference concerns the orange curve, representing the case with the installation further towards the bow. In off-design conditions, it appears that the pressure coefficient on the keel is not affected by the presence of the propulsive system installed in that position. The orange line, in fact, is quite superimposed on the black one, which corresponds to the isolated hull simulation.

3.3.3 ODW - Pressure distribution

The same analysis conducted on the hull's keel is also presented for the propulsor's external wall in the symmetry section, where the flow is more disturbed by the interaction with the hull.
In this investigation, since the installation position varies case by case, the axial non-dimensional coordinate is normalized by the following linear formula:

$$x/c = \frac{(x - min(x))}{(max(x) - min(x))} \tag{3.1}$$

The following figures represent the pressure coefficients along the external wall of the ODW, for the nearest (*"up"*) and the most distance (*"down"*) installation position under design conditions.

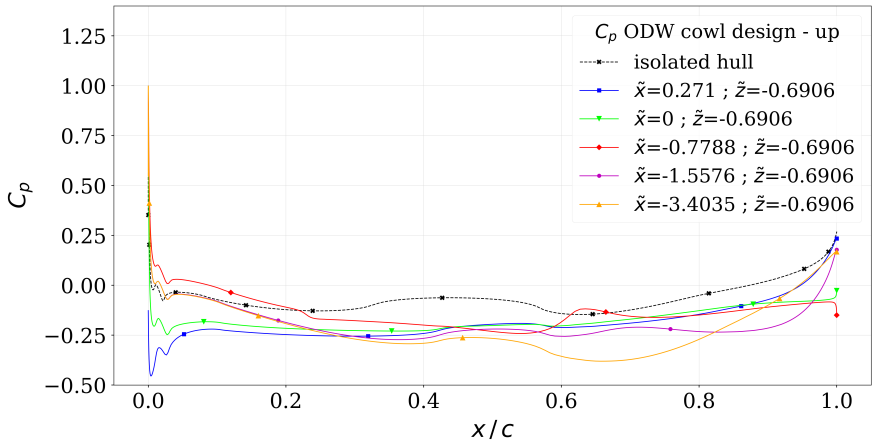

Figure 3.15: Pressure coefficient variation on the ODW's external cowl for varying longitudinal installation locations at vertical coordinate $z/D \geq -0.2969$, with an $IVR = 0.85$

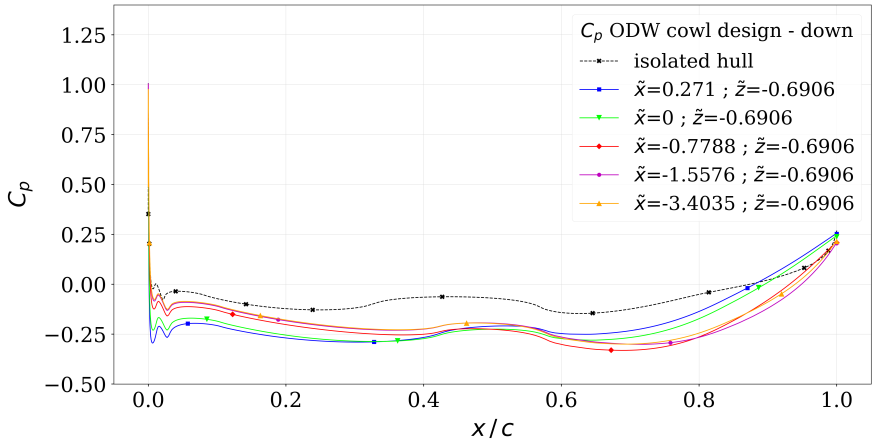

Figure 3.16: Pressure coefficient variation on the ODW's external cowl for varying longitudinal installation locations at vertical coordinate $z/D = -0.6909$, with an $IVR = 0.85$

In the first image 3.15, corresponding to the closest installation points, a much more perturbed pressure coefficient can be observed with respect to the second, 3.16, where the curves are much more stable and linear. By the analysis of the graphs, a common behaviour of the pressure coefficient emerges: at the coordinate $x/c = 0$, which corresponds to the leading edge of the inlet, a high C_p value indicates the stagnation point of the flow, also visible in Figure 3.5. A steep drop immediately after this point indicates a rapid acceleration, which reaches its maximum speed around $x/c \approx 0.4$, corresponding to the minimum cross section of the channel formed between

the hull and the propulsor. The flow then appears to remain stable until the converging section of the nozzle begins, which leads to a gradual widening of the Venturi channel, causing the flow to decelerate. This effect is reflected in the increase of C_p for axial coordinates $x/c > 0.6$. The values shown in the two images are comparable, but one main difference clearly stands out: while in the case with vertical coordinate $z/D = -0.6906$ (*"down"* cases) a full pressure recovery is always observed, reaching the reference value corresponding to the isolated case - black dashed line - in the case with a greater vertical coordinate, pressure recovery occurs only for certain installation positions, whereas in others, flow separation downstream of the propulsor is observed.

Figures 3.17 and 3.18 show the pressure coefficient distribution on the external walls of the waterjet under off-design conditions:

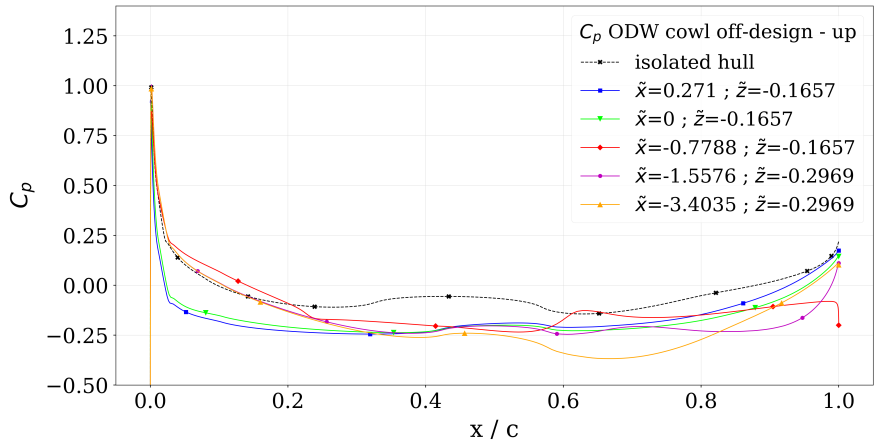

Figure 3.17: Pressure coefficient variation on the ODW's external cowl for varying longitudinal installation locations at vertical coordinate $z/D \geq -0.2969$, with an $IVR = 1.425$

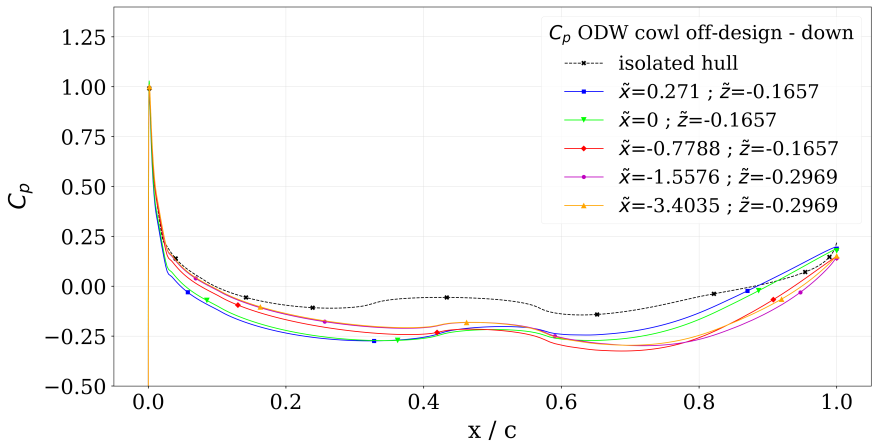

Figure 3.18: Pressure coefficient variation on the ODW's external cowl for varying longitudinal installation locations at vertical coordinate $z/D = -0.6909$, with an $IVR = 1.425$

This time, the differences with respect to the design condition are relative only to the first part of the propulsor, starting from the highlight to the external inlet, up to the coordinate $x/c < 0.2$. Further ahead this point, the behaviour is quite identical to that under the design condition.
Both Figures 3.17 and 3.18 are characterised by very high suction peaks occurring in the very first portion of the inlet highlight, explained by the cavitation phenomena that always occur under off-design conditions. However, this behaviour lasts for a very short part of the inlet, as a steep pressure recovery immediately follows, with C_p returning to positive values. This strong adverse pressure gradient, which ends at the stagnation point where the maximum pressure is reached, may lead to a significant deceleration of the flow, which boundary layer can potentially start to separate. However, the linear trend of the curve C_p observed after the initial part of the inlet suggests the presence of an attached laminar flow along the middle outer surface of the propulsor. Even in this case, C_p values remain below zero, indicating a flow acceleration along the outer wall of the propulsor.
When comparing the two images, referring to different vertical installation positions, it can be seen that the proximity to the hull disrupts the linear behaviour of C_p, which appears slightly more perturbed in Figure 3.17.
It is also particularly interesting to note that, under reduced speed conditions, pressure recovery at the rear end of the propulsor occurs for almost all installation configurations, with the exception of the one that experiences cavitation even under design conditions. In that specific case, a slight drop in C_p is observed in the nozzle exit section, indicating a re-acceleration of the flow.

3.4 Hull Forces

The following section is about reporting the results obtained on the hull. Forces are investigated for each ODW installation position, considering both the in-design and off-design configurations, and even in the isolated case. Because the hull simulation does not faithfully reproduce the physical reality, all the results are reported in comparison with the isolated case.

3.4.1 Hull - Drag

The drag is the hydrodynamic resistance, a force acting in the parallel direction with respect to the flow motion, and it opposes the forward progression of the hull.
The first investigation is conducted on the isolated hull, to elaborate the behaviour of the drag coefficient with increasing flow velocity, following the analysis of Figure 2.2. Three different operating points are considered: a take-off speed with velocity coefficient $v/V_{ref} = 0.3475$, the condition that coincides with the *hump* point with $v/V_{ref} = 0.4375$, and the cruise condition in which the velocity coefficient is equal to 1. The drag coefficient is calculated using the formula 2.7, where the reference area is the projected area of the hull, while the reference velocity equals the cruising speed. In the following Figure 3.19 the drag coefficient curve is reported with respect to the velocity coefficient $v/V_{ref} = C_v$, where V_{ref} equals the cruise speed.

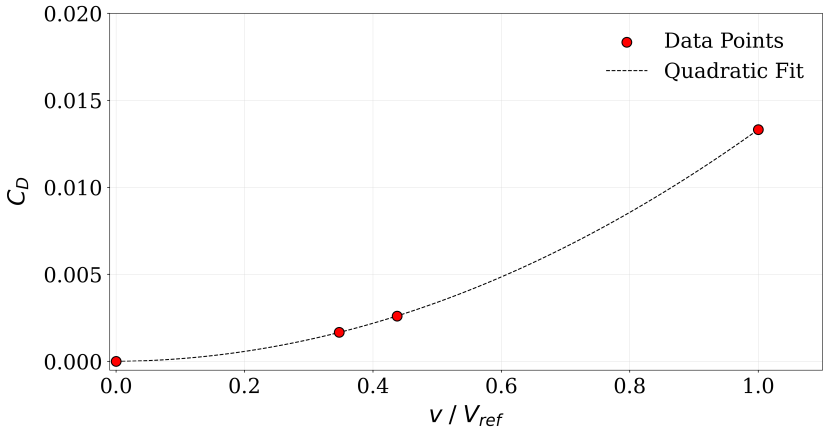

Figure 3.19: Drag coefficient of the isolated hull

It is clear that this curve differs from the drag coefficient of the planing hull, whose behaviour is investigated in Section 2.3. The main difference regards the first part of the curve, where there is no *hump* and the increment is a classical quadratic monotonic function. The explanation of these differences is quite simple: the simulation domain is fixed, the hull's bow does not lift, and the water surface does not create the bow wave. Therefore, this prediction-drag analysis has a "realistic" behaviour only for the speed coefficient $C_v > 0.75$.

The focus now moves to the hull on which the Outboard Dynamic-inlet Waterjet is installed. The drag results obtained by the simulations in both design and off-design are presented in the following Table 3.4 depending on the installation position and expressed through the non-dimensional coefficient C_D (equation 2.7), where V_{ref} equals the design and off-design velocity, respectively, and A_{ref} corresponds to the hull projected area.

Configuration	$\mathbf{C_D}_{\mathbf{hull}}^{\text{design}}$	$\mathbf{C_D}_{\mathbf{hull}}^{\text{off-design}}$
isolated hull	0.01331918	0.01361237
$0.271\ ;\ -0.1657$	0.01172129	0.01146669
$0.271\ ;\ -0.4282$	0.01203607	0.01183052
$0.271\ ;\ -0.6906$	0.01214201	0.01204132
$0\ ;\ -0.1657$	0.01182631	0.01146734
$0\ ;\ -0.4282$	0.0121541	0.01186373
$0\ ;\ -0.6906$	0.01222372	0.01207032
$-0.7788\ ;\ -0.16576$	0.01220021	0.0124967
$-0.7788\ ;\ -0.4282$	0.01228222	0.01215965
$-0.7788\ ;\ -0.6906$	0.0122771	0.01218918
$-1.5576\ ;\ -0.2969$	0.01134323	0.01154992
$-1.5576\ ;\ -0.6906$	0.01144382	0.01154729
$3.4035\ ;\ -0.2969$	0.0105943	0.01074818
$3.4035\ ;\ -0.6906$	0.01083005	0.01096711

Table 3.4: Drag forces for each ODW installation position in both design and off-design conditions.

The numerical analysis is then completed by reporting the colour map that illustrates the variation of the *'delta'* drag coefficient between the stand-alone hull and the case with the propulsor installed, depending on the vertical and horizontal displacement of the ODW. The $\Delta C_{D\,hull}$ is calculated as the difference between the force generated in the case with the installed propulsor and the force generated by the single hull:

$$\Delta D_{hull} = D_{hull\ installed} - D_{hull\ isolated} \tag{3.2}$$

which is then made dimensionless using the standard formula:

$$\Delta C_{D\,hull} = \frac{2 \cdot \Delta D_{hull}}{\rho\, A_{ref}\, V_{ref}^2} \tag{3.3}$$

In Figures 3.20 and 3.21 $\Delta C_{D\,hull}$ is shown for both the in-design and out-of-design Inlet Velocity Ratio.

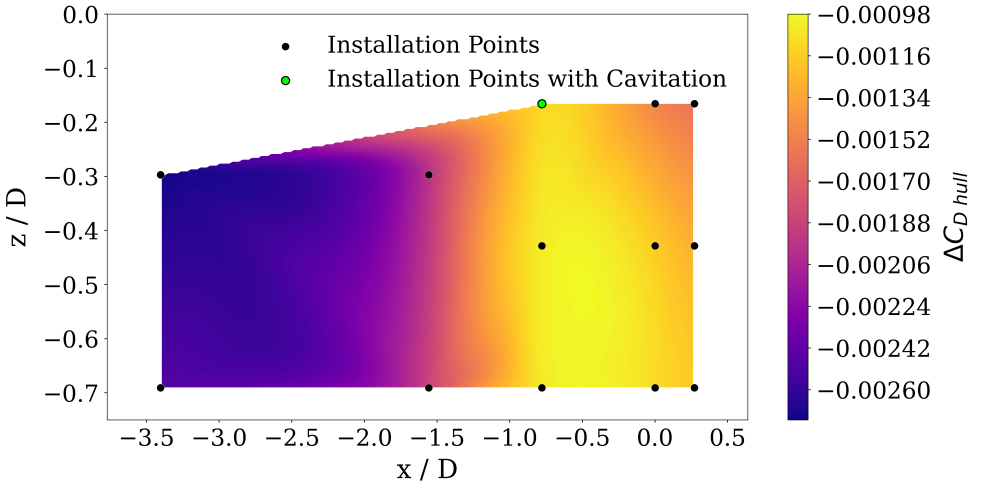

Figure 3.20: Influence of the installation position on the hull drag coefficient for IVR=0.85

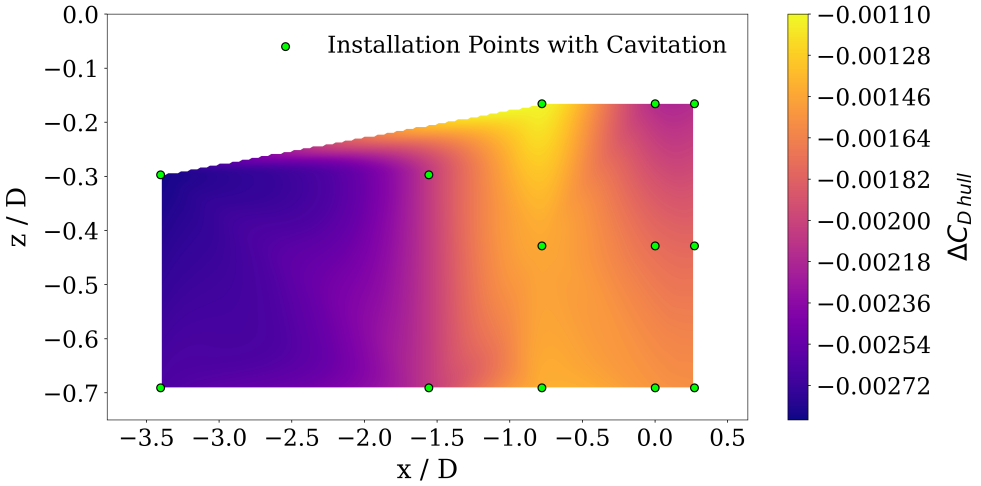

Figure 3.21: Influence of the installation position on the hull drag coefficient for IVR=1.425

In Figure 3.20 the values of $\Delta C_{D\,hull}$ are reported and the negative sign can be observed. Given the definition of this parameter in Equation 3.3, the negative value indicates that, under the design conditions, the installation of the propulsive system contributes positively, reducing the hydrodynamic resistance of the hull.
In Figure 3.21, the colour map of the hull drag coefficient is shown for the off-design condition. Comparing these results with the design case, it is clear that the two act in a very similar way. In this condition, the presence of the propulsive system is even more beneficial: the difference in drag coefficient is, in fact, slightly lower.

Examining the colour maps, it is evident that more forward engine installations result in more negative drag coefficients, meaning that the presence of the propulsor has a beneficial effect compared to a more aft position. From a physical perspective, this behaviour can be explained by the fact that the propulsor, drawing in the water, speeds up, energises, and makes the hull's boundary layer thinner, and the resistance decreases. The results show that the smallest drag reduction contribution occurs at an axial coordinate of approximately $x/D \approx -0.75$. Then a further improvement is observed for the most rearward positions, particularly when closer to the hull's keel projection. It is also interesting to observe that for an installation position with an axial coordinate smaller than -0.5 (i.e., when the ODW highlight is well below the hull), there are small variations in $\Delta C_{D\,hull}$ along the vertical direction.

3.4.2 Hull - Lift

The second force acting on the hull is the vertical force. It is initially composed of hydrostatic buoyancy, but as the speed increases, also a hydrodynamic lift component arises. This force reduces the pitch of the hull and reduces the drag, leading to a planing regime that depends on the forward velocity, the shape of the hull and the environmental conditions. The hydrostatic buoyancy force to which the hull is subjected, according to Archimedes' principle, is equal to the weight of the displaced fluid and enables flotation even when in motion. However, as velocity increases, the fluid pressure distribution around the hull changes, altering the vertical force.
The following Table 3.5 presents the vertical forces acting on the hull for the different ODW installation points, expressed in the non-dimensional form with the lift coefficient C_L, obtained by using the same reference velocities and the same reference hull projected area.

Configuration	$\mathbf{C_{L\,hull}^{\text{design}}}$	$\mathbf{C_{L\,hull}^{\text{off-design}}}$
isolated hull	-0.053931	-0.05425675
$0.271\ ;\ -0.1657$	-0.04908774	-0.0529768
$0.271\ ;\ -0.4282$	-0.04976643	-0.05315615
$0.271\ ;\ -0.6906$	-0.0506559	-0.05335803
$0\ ;\ -0.1657$	-0.04810973	-0.05258147
$0\ ;\ -0.4282$	-0.04899953	-0.05275412
$0\ ;\ -0.6906$	-0.05019125	-0.05309351
$-0.7788\ ;\ -0.16576$	-0.04598478	-0.05020691
$-0.7788\ ;\ -0.4282$	-0.04770608	-0.05122798
$-0.7788\ ;\ -0.6906$	-0.04947341	-0.05228343
$-1.5576\ ;\ -0.2969$	-0.05264104	-0.05477922
$-1.5576\ ;\ -0.6906$	-0.05294538	-0.05496096
$-3.4035\ ;\ -0.2969$	-0.05836715	-0.06017556
$-3.4035\ ;\ -0.6906$	-0.05595223	-0.05776944

Table 3.5: Lift coefficients for each ODW installation position in design and off-design conditions.

The negative sign of the lift values indicates that the force acts downward, resulting in a kind of hydrodynamic downforce. The hull can, in fact, be considered as an inverted airfoil, generating a low-pressure field and thus creating a suction effect.
Having a higher lift force component can be advantageous, because it reduces the hull's wetted area and the draft, leading to lower hydrodynamic resistance. Even in this analysis, the lift in the stand-alone condition is subtracted from the lift of the hull with the propulsor installed and then is made non-dimensional:

$$\Delta L_{hull} = L_{hull\,installed} - L_{hull\,isolated} \tag{3.4}$$

$$\Delta C_{L\,hull} = \frac{2 \cdot \Delta L_{hull}}{\rho\, A_{ref}\, V_{ref}^2} \tag{3.5}$$

where the force perpendicular to the flow direction L_{hull} is obtained from the simulations, the reference velocity V_{ref} is equal to the cruise and slow-speed condition, while the reference area A_{ref} corresponds to the hull's projected area.
In Figures 3.22 and 3.23 the hull lift coefficients $\Delta C_{L\,hull}$ are reported for each installation point.

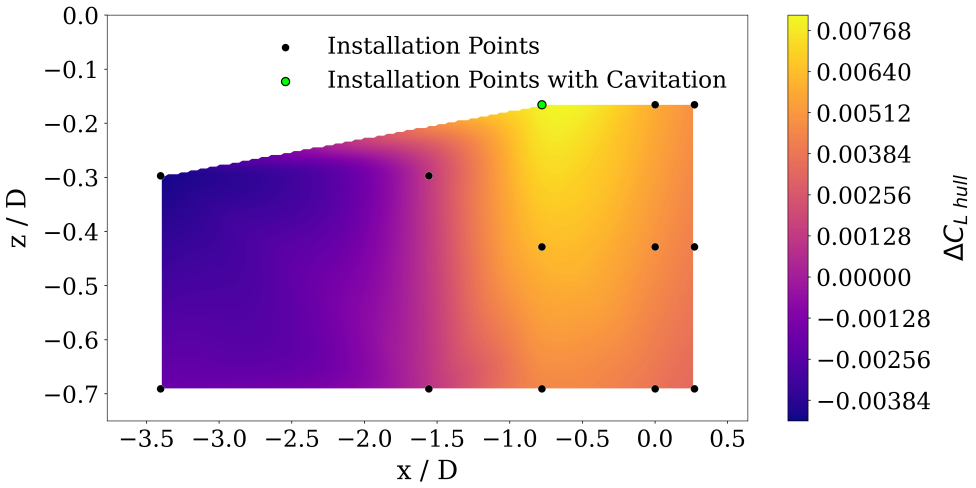

Figure 3.22: Influence of the installation position on the hull lift coefficient for IVR=0.85

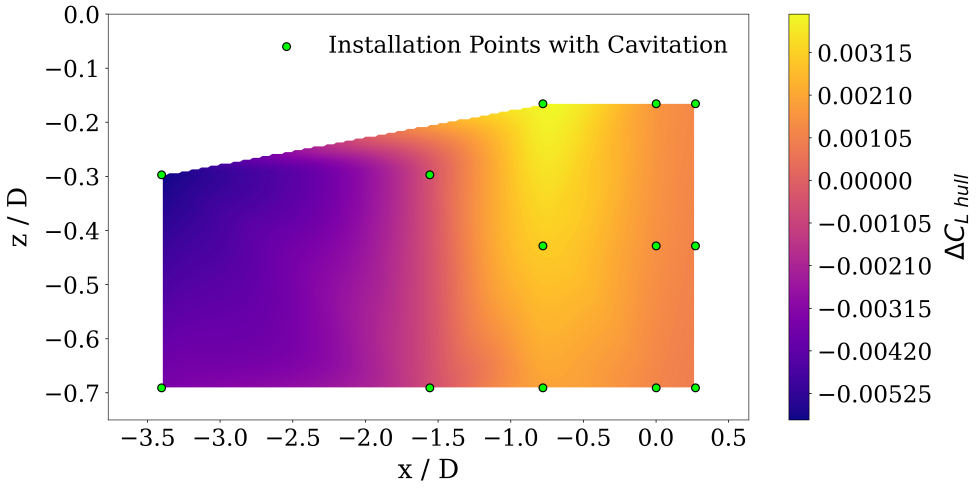

Figure 3.23: Influence of the installation position on the hull lift coefficient for IVR=1.425

The positive values reported for the installation positions to the right of the axial coordinate $x/D \approx -1.5$ suggest that the engine contributes favourably to the generation of an upward lifting force on the hull. This is because, according to Equation 3.4 and given that the lift forces for both the installed and isolated configurations are negative ($L_{hull\,installed}$, $L_{hull\,isolated} < 0$), a positive result means that:

$$|L_{hull,isolated}| > |L_{hull,installed}| \tag{3.6}$$

In other words, the presence of the engine acts as an obstacle for the motion of the flow, that slows down increasing the local pressure and thereby reducing the magnitude of the downward force.

To the left of the aforementioned point, a negative difference in the lift coefficient occurs, indicating that the engine contributes to an increase in the downforce generated by the hull. From a qualitative point of view, this behaviour may be explained by the formation of a sort of Venturi channel between the upper surface of the propulsor and the keel of the hull. In this region, the flow is forced through a converging passage, resulting in an increasing velocity and a corresponding drop in pressure, which is responsible for the condition $\Delta C_{L\,hull} < 0$.

A similar behaviour is observed in 3.23 under lower speed conditions, as the two figures appear almost identical. What changes are the values of lift difference relative to the isolated case. In this configuration, the maximum positive difference is reduced, while the negative difference increases. As a result, the off-design installation further deteriorates the hydrodynamic characteristics of the hull.

In the end, the optimal installation configuration occurs along the longitudinal position corresponding to an axial coordinate of approximately $x/D \approx -0.75$, while the most favourable vertical position is the closest to the hull.

3.5 Outboar Dynamic-inlet Waterjet Forces

Given the effects observed on the hull, it is also crucial to examine how the installation position influences the dynamics of the propulsion system. A detailed understanding of the hydrodynamic forces acting on the engine across many different trim configurations and operating conditions is essential not only for a better comprehension of the system, but it is also fundamental for the design of structural components, such as engine mounts, for example. This particular aspect is very relevant since the propulsor has an entirely outboard configuration.
In line with the hull analyses, even the ODW results are reported with respect to the isolated simulation. This choice comes from the non-physical condition on which the propulsor is installed. In a real case, in fact, the propulsive system is influenced not only by its installation position, but also by the trim of the planing boat or its configuration with respect to the fluid flow. So, it is convenient to identify a common reference base on which to calculate the differences.

3.5.1 ODW - Drag

This section investigates the drag forces acting on the propulsor. Specifically, the so-called nacelle drag (D_{nac}), a parameter directly derived from the aerospace field [3], is analysed. Its formulation is obtained by combining equations 2.6 and 2.8, resulting in:

$$D_{nac} = FG2 - FG0 + \theta_{int} + \theta_{sp} + \phi_{nac} \tag{3.7}$$

from which, including equation 2.14:

$$D_{nac} = FG2 - FG0 + NF \tag{3.8}$$

Considering the definition of the gauge force in equation 2.5, it is possible to compute $FG2$ from integrating over the pump face area the following expression directly in Fluent:

$$FG_2 = \iint \left[(p_2 - p_\infty) + \rho \cdot u \cdot u\right] \, dA \tag{3.9}$$

where p_2 is the static pressure at the pump face, p_∞ is the atmospheric pressure and u corresponds to the flow axial velocity. $FG0$ then can be easily calculated as: $FG0 = \dot{m}\, V_{ref}$, where $\dot{m}$ is the mass flow rate that depends on the cruise condition.

Using this method, the results reported in Table 3.6 are computed and expressed in their non-dimensional form using the usual equation, in which the reference area is the inlet pump face area and the velocity is equal to the design and off-design conditions, respectively.

Configuration	$\mathbf{C_{D\,nac}}^{\text{design}}$	$\mathbf{C_{D\,nac}}^{\text{off-design}}$
isolated ODW	0.09755532	0.19531722
$0.271\ ;\ -0.1657$	0.02460809	0.19008901
$0.271\ ;\ -0.4282$	0.02848853	0.17174591
$0.271\ ;\ -0.6906$	0.02146853	0.16832588
$0\ ;\ -0.1657$	0.10221255	0.23314977
$0\ ;\ -0.4282$	0.0812994	0.21389333
$0\ ;\ -0.6906$	0.05358815	0.21438876
$-0.7788\ ;\ -0.16576$	0.21916122	0.33180272
$-0.7788\ ;\ -0.4282$	0.2037266	0.32557121
$-0.7788\ ;\ -0.6906$	0.15884177	0.28968211
$1.5576\ ;\ -0.2969$	0.23686848	0.36705478
$1.5576\ ;\ -0.6906$	0.19737105	0.32704719
$-3.4035\ ;\ -0.2969$	0.22676765	0.36164166
$-3.4035\ ;\ -0.6906$	0.18208336	0.31122915

Table 3.6: ODW drag forces for each ODW installation position in design and off-design conditions.

The following Figures 3.24 and 3.25 show the colour map of the nacelle drag coefficient during cruise and off-design conditions. Even in this analysis the reported data are not expressed as absolute values, but they are computed with respect to the isolated ODW case, and then make dimensionless.

$$\Delta D_{nac} = D_{nac}^{installed} - D_{nac}^{isolated} \tag{3.10}$$

$$\Delta C_{D\,nac} = \frac{\Delta D_{nac}}{0.5\,\rho\,A_{ref}\,V_{ref}^2} \tag{3.11}$$

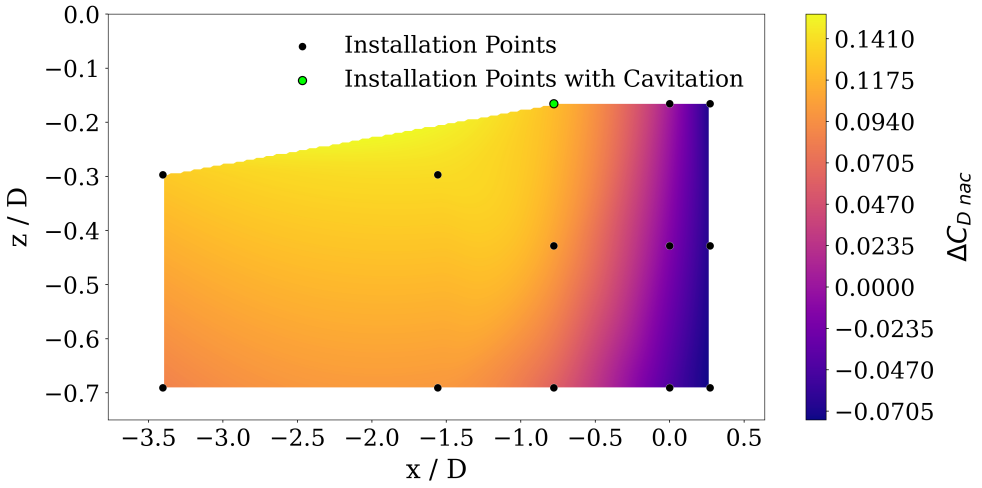

Figure 3.24: Installation position influence on the nacelle drag coefficient with respect the isolated case for IVR=0.85

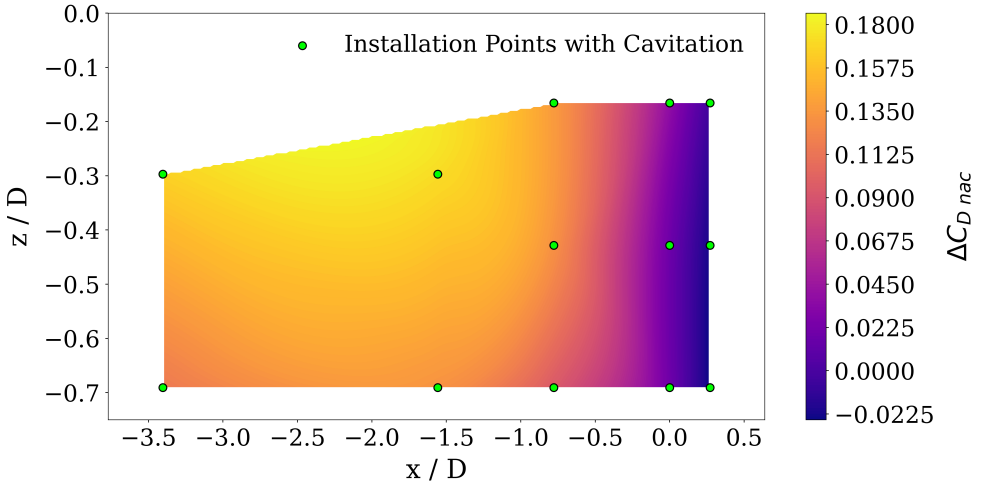

Figure 3.25: Installation position influence on the nacelle drag coefficient with respect the isolated case for IVR=1.425

The two images appear very similar, indicating a behaviour that does not change significantly between the nominal design and the off-design condition.
A positive value of $\Delta C_{D\,nac}$, as defined by ΔD_{nac} in Equation 3.10, indicates that the installation positions contribute negatively to the drag of the propulsor. Since $D_{nac} > 0$, as reported in Table 3.6, a positive value of $\Delta C_{D\,nac}$ implies that $D_{nac}^{installed} > D_{nac}^{isolated}$. This condition occurs in most of the operating domain defined by the analysed installation positions, as shown in the figures by the yellow and orange regions. In particular, the most unfavourable conditions are

those in which the engine is installed in more forward positions and closer to the hull.
In contrast, there are also regions where the phenomenon behaves oppositely, where $\Delta C_{D\ nac} < 0$. In both operating conditions, the installation points, where a lower resistance is observed than in the isolated case, are located outside the hull's trailing edge outline, i.e., in positions with coordinate $x/D < 0$. From a phenomenological perspective, this effect may be attributed to the turbulent wake generated in the stern region of the hull, which helps to reduce the drag acting on the propulsor by delaying boundary layer separation. Physically, the wake generated by the hull promotes the development of a turbulent boundary layer that, compared to the laminar one, enables greater momentum exchange with the outer flow region and, therefore, has a higher energy. This results in delayed flow separation, with the separation point shifting downstream, reducing the wake width, and consequently the pressure drag.
One noticeable difference arising from the comparison of the two figures is that, as expected, the design condition offers more favourable outcomes than the off-design cases. Specifically, both the maximum and minimum values of $\Delta C_{D\ nac}$ are lower in the design scenario, which translates into improved efficiency.

3.5.2 ODW - Lift

In addition to the force acting in the longitudinal direction of the flow, the propulsion unit experiences an additional force perpendicular to the undisturbed flow, which is referred as lift. During this analysis, the lift coefficients are not reported with respect to a reference value because the isolated ODW is simulated using a 2D axial-symmetric geometry with no resultant vertical force components.
In the complete problem, the lift force is generated by the asymmetrical and non-homogeneous pressure distribution around the propulsion unit, due to the mutual interaction between the hull and the waterjet installation position that modifies the water flow on the upper engine cowl. This phenomenon leads to the generation of the aforementioned vertical force.
In Table 3.7 the lift forces generated by the propulsive system for different installation positions are reported in their non-dimensional form, with the usual reference parameter.

Configuration	$C_{L\ \text{jet}}^{\text{design}}$	$C_{L\ \text{jet}}^{\text{off-design}}$
0.271 ; −0.1657	0.1731165	0.25693642
0.271 ; −0.4282	0.21440807	0.25397209
0.271 ; −0.6906	0.20833915	0.23466605
0 ; −0.1657	0.08371634	0.22644097
0 ; −0.4282	0.19996864	0.24295547
0 ; −0.6906	0.20819182	0.23038747
−0.7788 ; −0.16576	-0.11281865	-0.05169689
−0.7788 ; −0.4282	0.12729178	0.15018221
−0.7788 ; −0.6906	0.17567308	0.18864843
1.5576 ; −0.2969	0.06940032	0.05941666
1.5576 ; −0.6906	0.10379229	0.1043942
−3.4035 ; −0.2969	0.16495891	0.1522032
−3.4035 ; −0.6906	0.08982765	0.08745783

Table 3.7: ODW lift for each installation position

The following Figures 3.26 and 3.27 illustrate the variation of the lift generated by the Outboard Dynamic-inlet Waterjet as a function of his installation position, expressed in terms of dimensionless lift coefficient:

$$C_{L\ \text{ODW}} = \frac{\sum_{i=1}^{N} L_i}{0.5\,\rho\,A_{ref}\,V_{ref}^2} \tag{3.12}$$

where L_i is the lift generated by i-part of the engine. The reference velocities remain unchanged as the reference pump face area.

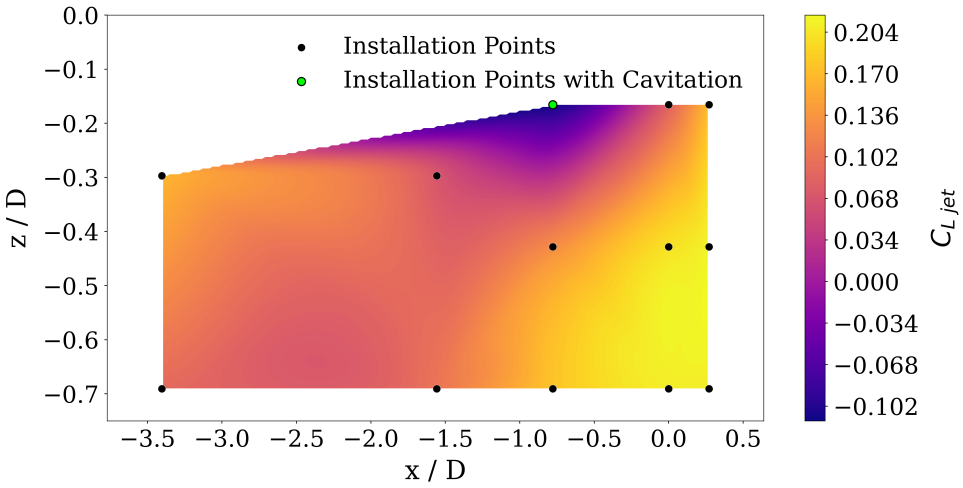

Figure 3.26: ODW lift coefficient distribution depending on the installation position for IVR=0.85

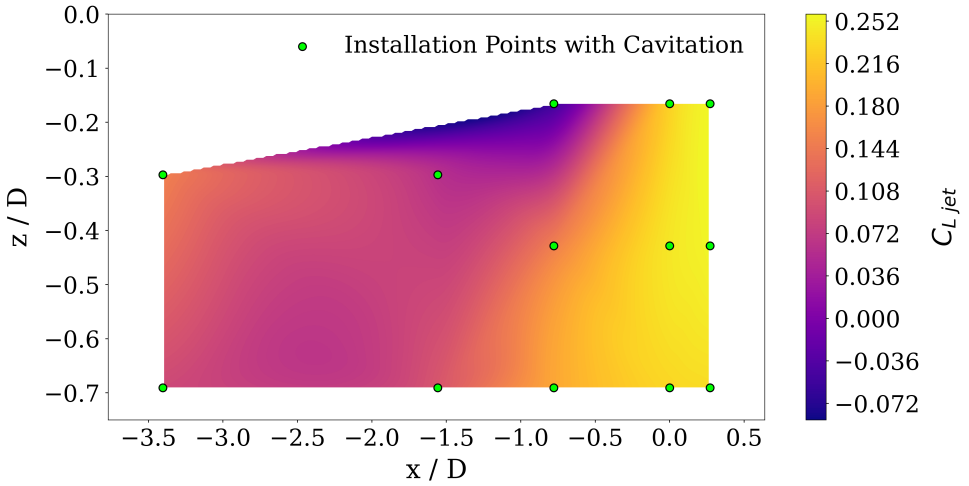

Figure 3.27: ODW lift coefficient distribution depending on the installation position for IVR=1.425

The analysed vertical force includes, in addition to the hydrodynamic force exerted by the fluid on the propulsor, the hydrostatic thrust described by the buoyancy Archimedes' principle, which constantly acts upward.
In almost all installation positions, a positive lift coefficient is observed, indicating a net contribution of lift to the system. One main difference between the behaviour of the two conditions can be identified: in Figure 3.26, the maximum lift coefficient occurs at the most aft and farthest position from the hull; in the off-design condition, shown in Figure 3.27, the highest lift coefficient is recorded at the same longitude, but at a location closer to the keel.
Among all the configurations analysed, only one exhibits a negative lift coefficient. This corresponds to the installation point affected by the cavitation phenomena, identified by the coordinates $x/D = -0.77880$ and $z/D = -0.1657$. It is interesting to note that, contrary to what might be expected, the most favourable condition could actually correspond to the installation position just mentioned. Although the goal should be maximising the upward lift in order to reduce the wetted surface of the hull and consequently its hydrodynamic resistance, it is important to consider the moments generated around the centre of gravity of the system.
The analysed hull has a planing-type configuration, and considering that the system's centre of gravity is likely located in a more forward position than the pressure centre of the propulsor, the most beneficial condition is the one in which the lift contribution is negative. So, the generated moment helps to pitch-up the planing hull's bow, thereby reducing water friction and providing an overall advantage to the system.

3.5.3 ODW - Net Propulsive Thrust

The focus of the analysis now moves to one of the most influential parameters in the context of propulsion: the Net Propulsive Thrust. This quantity defines the thrust that the propulsive

system provides to the vessel under different operating conditions, based on the propulsive and resistive forces acting within and outside the domain represented in Figure 2.1. Recalling Equations 2.15 and 2.14, the NPT is defined as:

$$NPT = FG2 - FG_9 + NF \tag{3.13}$$

where NF is the nacelle force, given by the contribution of the external cowl, spinner and intake forces, while $FG2$ and $FG9$ represent respectively the gauge forces at the inlet and outlet of the axial pump.
The following tables present the results of the quantities involved under both design and off-design conditions. The reported values are made non-dimensional by using the usual formula:

$$C_F = \frac{2 \cdot F}{\rho \, A_{ref} \, V_{ref}^2} \tag{3.14}$$

where F is the generic force, A_{ref} is the pump-inlet area and V_{ref} the reference velocities under design and off-design.

Configuration	$\mathbf{C}_{\mathbf{NF}}^{\text{design}}$	$\mathbf{C}_{\mathbf{NF}}^{\text{off-design}}$
isolated ODW	-0.0708307	0.16075864
0.271 ; -0.1657	-0.09919578	0.29586707
0.271 ; -0.4282	-0.10538199	0.29257064
0.271 ; -0.6906	-0.10980684	0.29257712
0 ; -0.1657	-0.0681909	0.31796868
0 ; -0.4282	-0.07919231	0.31287818
0 ; -0.6906	-0.09061026	0.30826709
-0.7788 ; -0.16576	–0.00976434	0.37484837
-0.7788 ; -0.4282	-0.01806975	0.37274479
-0.7788 ; -0.6906	-0.04114958	0.35508293
1.5576 ; -0.2969	-0.00192726	0.39519173
1.5576 ; -0.6906	-0.02193527	0.3748568
-3.4035 ; -0.2969	-0.00690868	0.39257336
-3.4035 ; -0.6906	-0.02974781	0.36712872

Table 3.8: Nacelle Force (NF) for different installation positions.

By analysing the data reported in Table 3.8 it is interesting to observe the difference between the design and off-design condition. The negative sign characterises the design condition in the first column, and it indicates that the force distribution developed on the walls of the propulsor positively contributes to the thrust rather than acting as a classical resistance. This effect is mainly due to the internal section of the intake, which generates a force that varies with the installation position. Physically, this behaviour is a consequence of the "channel" shape formed within the engine's inlet. The carefully designed inlet and spinner geometries create a region of pressure lower than the external one, resulting in a suction of the flow that is revealed as a forward thrust.

The next tables report the values of the non-dimensional gauge forces at the pump outlet and inlet, respectively.

Configuration	$\mathbf{C}_{\mathbf{FG9}}^{\text{design}}$	$\mathbf{C}_{\mathbf{FG9}}^{\text{off-design}}$
isolated ODW	1.8229718	5.0067912
$0.271\ ;\ -0.1657$	1.7983242	4.93106986
$0.271\ ;\ -0.4282$	1.80967104	4.94027988
$0.271\ ;\ -0.6906$	1.81387026	4.94335254
$0\ ;\ -0.1657$	1.76450178	4.9220472
$0\ ;\ -0.4282$	1.80178148	4.93342462
$0\ ;\ -0.6906$	1.8085749	4.93808097
$-0.7788\ ;\ -0.16576$	1.69615148	4.83662608
$-0.7788\ ;\ -0.4282$	1.78008086	4.91190593
$-0.7788\ ;\ -0.6906$	1.79406588	4.92401286
$1.5576\ ;\ -0.2969$	1.76667947	4.89632908
$1.5576\ ;\ -0.6906$	1.78486011	4.91446313
$-3.4035\ ;\ -0.2969$	1.7781798	4.90774318
$-3.4035\ ;\ -0.6906$	1.78882013	4.91846277

Table 3.9: Gauge forces at the pump exit ($FG9$) for different installation positions

Configuration	$\mathbf{C}_{\mathbf{FG2}}^{\text{design}}$	$\mathbf{C}_{\mathbf{FG2}}^{\text{off-design}}$
isolated ODW	1.2231482	1.6021808
$0.271\ ;\ -0.1657$	1.22367713	1.63293517
$0.271\ ;\ -0.4282$	1.22375542	1.62875998
$0.271\ ;\ -0.6906$	1.22493909	1.62623094
$0\ ;\ -0.1657$	1.22431339	1.63178794
$0\ ;\ -0.4282$	1.22399036	1.62885778
$0\ ;\ -0.6906$	1.22490431	1.62627655
$-0.7788\ ;\ -0.16576$	1.22415296	1.61757264
$-0.7788\ ;\ -0.4282$	1.22374167	1.62199477
$-0.7788\ ;\ -0.6906$	1.22472886	1.62214272
$1.5576\ ;\ -0.2969$	1.22450644	1.61736922
$1.5576\ ;\ -0.6906$	1.22463292	1.61988283
$-3.4035\ ;\ -0.2969$	1.22441073	1.6172506
$-3.4035\ ;\ -0.6906$	1.22486793	1.61960347

Table 3.10: Gauge forces coefficient at the pump face ($FG2$) for different installation positions

Based on the results reported and applying Equation 3.13, it is finally possible to present in Table 3.11 the values of NPT under both design and off-design conditions, now referring to the entire propulsor rather than only one half.

Configuration	$\mathbf{C_{NPT}^{design}}$	$\mathbf{C_{NPT}^{off\text{-}design}}$
isolated ODW	-0.67065442	-3.08309313
$0.271\ ;\ -0.1657$	-0.67384285	-3.00226762
$0.271\ ;\ -0.4282$	-0.69129761	-3.01894926
$0.271\ ;\ -0.6906$	-0.698738	-3.02454449
$0\ ;\ -0.1657$	-0.60837928	-2.97229058
$0\ ;\ -0.4282$	-0.65698344	-2.99168866
$0\ ;\ -0.6906$	-0.67428084	-3.00353733
$-0.7788\ ;\ -0.16576$	-0.47988184	-2.84420508
$-0.7788\ ;\ -0.4282$	-0.57440893	-2.91716638
$-0.7788\ ;\ -0.6906$	-0.6104866	-2.94678721
$1.5576\ ;\ -0.2969$	-0.54410029	-2.88376813
$1.5576\ ;\ -0.6906$	-0.58216246	-2.9197235
$-3.4035\ ;\ -0.2969$	-0.56067775	-2.89791922
$-3.4035\ ;\ -0.6906$	-0.59370001	-2.93173058

Table 3.11: Net Propulsive Thrust NPT for different installation positions

The data reported are useful to compare the different case results, but they have no direct physical correspondence with the real-world scenario. This is primarily due to the conditions under which the simulations are carried out, where the effects of the wave motion, as well as the pitching and rolling of the vessel, are not considered.
However, by converting the force coefficient C_{NPT} into the corresponding Net Propulsive Thrust, the obtained results can be compared to the propulsor map shown in figure 2.2 and a certain consistency in the values can be observed. It is worth noting that, as described in Section 2.3, it is possible to obtain cruise thrust conditions that are comparable to the off-design results, and in some cases, the design NPT is even lower despite the significantly increased velocity.

To attribute some physical importance to the reported data, as was done for the previously performed analyses, it is necessary to compare the obtained results with those of the isolated ODW case. The following images show the difference in Net Propulsive Force between the installed and isolated cases, expressed as a dimensionless coefficient calculated as:

$$\Delta NPT = NPT_{installed} - NPT_{isolated} \tag{3.15}$$

$$\Delta C_{NPT} = \frac{2 \cdot \Delta NPT}{\rho\, A_{ref}\, V_{ref}^2} \tag{3.16}$$

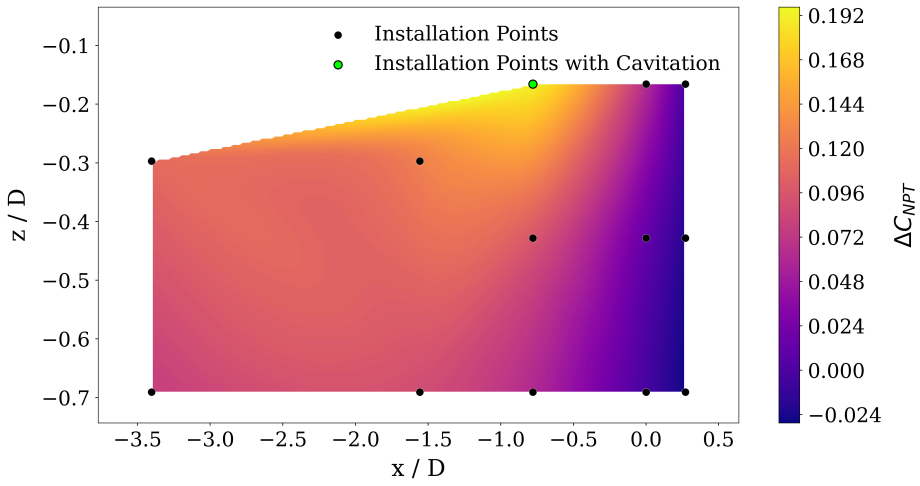

Figure 3.28: ODW Net Propulsive Force coefficient distribution depending on the installation position for IVR=0.85

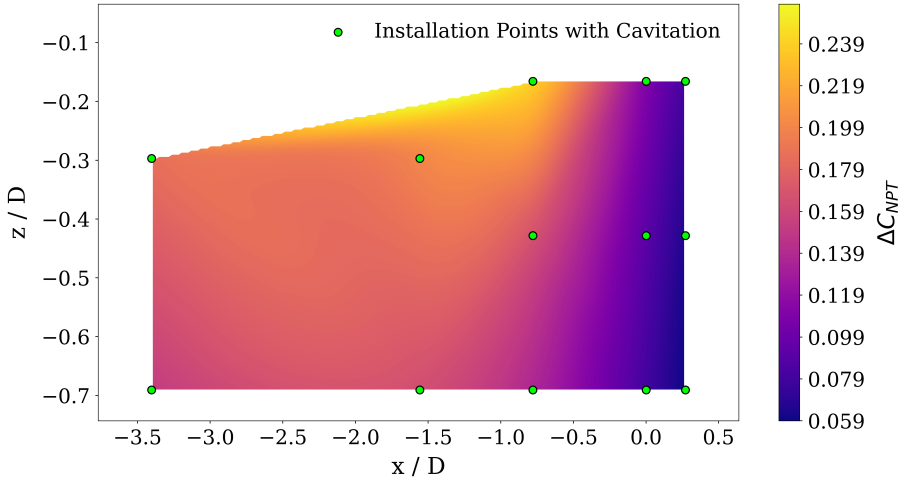

Figure 3.29: ODW Net Propulsive Force coefficeint distribution depending on the installation position for IVR=1.425

Based on the definition of ΔC_{NPT}, it follows that negative values of this parameter represent the most favourable condition, as they indicate that the mutual interaction between the hull and the propulsor has a positive effect on the forward thrust. Conversely, a positive value implies that $|NPT_{isolated}| > |NPT_{installed}|$, meaning that the effects of installation negatively impact the performance of the propulsor.
Figure 3.28 shows the design case, where ΔC_{NPT} is positive for most of the installation positions. The least favourable condition occurs when the propulsor is placed at $(x/D = 0\ ;\ z/D =$

-0.1657), the closest location to the hull, where the largest drop in thrust compared to the isolated case is observed. On the other hand, the most advantageous setup is found when the propulsor is installed at the farthest longitudinal distance from the hull, at coordinate $x/D = 0.271$, resulting in improved performance relative to the isolated configuration. This slight performance improvement trend is also visible in the vertical direction in some areas, where a gradual darkening of the colour map suggests a reduction in ΔC_{NPT} as the z/D coordinate decreases. The region where $\Delta C_{NPT} < 0$, highlighted by the dark purple colour, also appears to expand at its lower vertical positions.

The off-design case, shown in Figure 3.29, behaves much in the same way as the design condition. The main difference lies in the fact that no installation position yields an improvement over the isolated propulsor case; instead, a performance degradation is consistently observed. Indeed, ΔC_{NPT} is positive across all installation configurations.

From a phenomenological standpoint, the deterioration in propulsive performance - particularly in regions close to the hull - can be attributed to the interaction between the inflow and the boundary layer, or to disturbances caused by the presence of the hull. In the off-design condition, this degradation was more expected: the flow duct features a much wider free-stream inlet section that converges to the inlet's highlight. This configuration leads to an interaction between the incoming flow and the boundary layer of the hull, a portion of which is ingested by the propulsor. Since the flow entering the axial pump must be as stable and steady as possible, the ingestion of the boundary layer negatively affects the performance of the propulsor, ultimately reducing its efficiency.
In addition to these causes, the presence of cavitation bubbles should not be neglected, as they further disturb the pump inflow. Therefore, the off-design condition can be considered particularly critical, as it can lead to severe issues that threaten the operational life of the waterjet, as discussed in more detail in Section 2.4.

3.6 Net Vehicle Force

The final and most significant parameter analysed is the Net Vehicle Force (NVF). This force, calculated as described in Equation 2.16, represents the net force acting on the vessel.
In Table 3.12 the dimensionless net vehicle force coefficients corresponding to the NVF for both the design and off-design cases are reported and calculated using Equation 3.14.

Configuration	$\mathbf{C}_{\mathbf{NVF}}^{\text{design}}$	$\mathbf{C}_{\mathbf{NVF}}^{\text{off-design}}$
isolated ODW	1.25866157	-1.111309
$0.271\ ;\ -0.1657$	0.23349408	-2.68257978
$0.271\ ;\ -0.4282$	0.23991069	-2.61054098
$0.271\ ;\ -0.6906$	0.24171341	-2.56066018
$0\ ;\ -0.1657$	0.25188957	-2.62243876
$0\ ;\ -0.4282$	0.25163352	-2.54639775
$0\ ;\ -0.6906$	0.24998872	-2.51024492
$-0.7788\ ;\ -0.16576$	0.2935388	-2.06805811
$-0.7788\ ;\ -0.1657$	0.27469351	-2.31162395
$-0.7788\ ;\ -0.6906$	0.26629803	-2.36231055
$1.5576\ ;\ -0.2969$	0.25059072	-2.42146907
$1.5576\ ;\ -0.6906$	0.24523422	-2.49414208
$-3.4035\ ;\ -0.2969$	0.22207438	-2.68203932
$-3.4035\ ;\ -0.6906$	0.22233138	-2.68623709

Table 3.12: Net Vehicle Force NVF for different installation positions

The design data reported in the table further demonstrate the lack of physical correspondence between the simulated problem and the real-world scenario. In fact, under design conditions, a positive net thrust coefficient is observed, which corresponds to a backward motion, clearly incompatible with the actual under investigation condition.
This situation results primarily from the "static" simulation of the planing hull, as previously discussed in Section 3.4, which leads to a drag coefficient significantly higher than what would be expected in practice.
From the definition of the NVF:

$$NVF = NPT\ +\ \phi_{hull} \tag{3.17}$$

if the $NPT < 0$ and the drag of the hull in the design condition is much higher than the actual resistance acting on the hull surfaces, the resulting value of NVF becomes positive.
The off-design condition, instead, proves to be much more realistic, as the net thrust is negative, which is consistent with the forward motion of the boat. This outcome can be attributed to the hull planing configuration, which at lower speeds is characterised by a significantly larger wetted surface compared to the design condition, where the pitch angle is higher. As a result, there is a greater similarity between the isolated geometry and the actual physical case.

From these considerations, even the results reported in the following paragraphs, on the determination of the optimal installation position, refer to the difference between the NVF obtained from the simulations and that of the ideal case, in which the isolated hull and propulsor are considered together. The equations describing the adopted procedure are reported below:

$$\Delta NVF = NVF_{installed} - NVF_{isolated} \tag{3.18}$$

where the $NVF_{isolated} = NPF_{isolated} + \phi_{hull\ isolated}$.
Finally the non-dimensional force coefficient is:

$$\Delta C_{NVF} = \frac{2 \cdot \Delta NVF}{\rho\, A_{ref}\, V_{ref}^2} \tag{3.19}$$

In Figures 3.30 and 3.31 the colormaps represent the ΔC_{NVF} values depending on the variation of the installation positions.

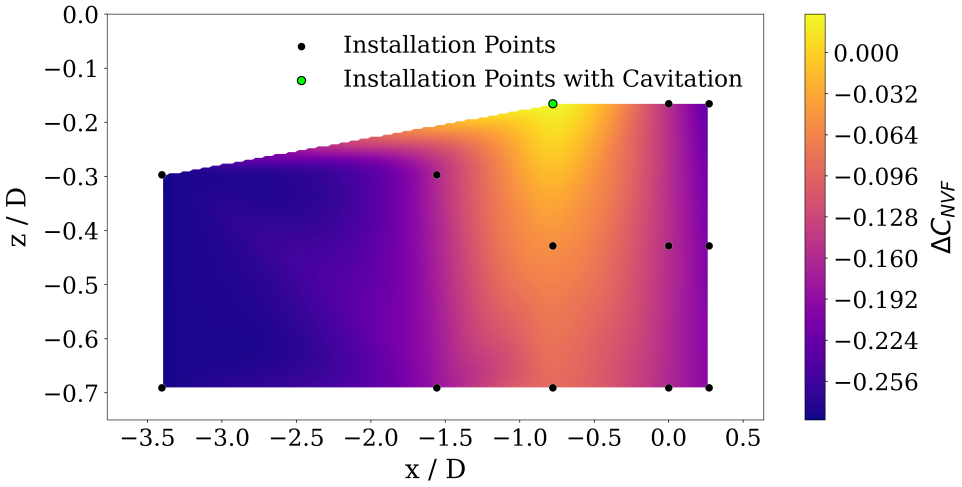

Figure 3.30: Influence of the installation position on the Net Vehicle Force coefficient for IVR=0.85

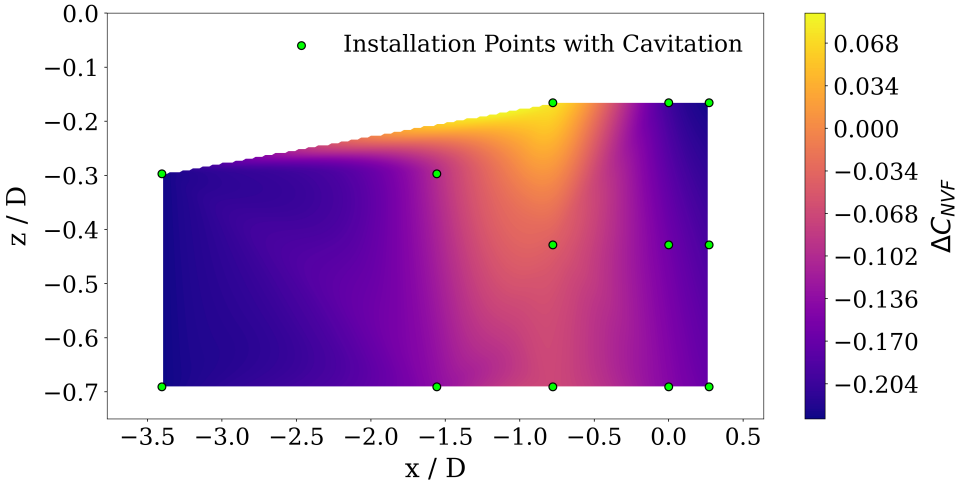

Figure 3.31: Influence of the installation position on the Net Vehicle Force coefficient for IVR=1.425

Starting from Equation 3.18, it can be seen that in both design and off-design conditions, the

optimal configuration is the one in which the ΔC_{NVF} is as negative as possible.
Although the values obtained during high-speed cruise are not particularly meaningful, the most favourable condition is the one in which a smaller net force is observed in the direction opposite to the motion and this corresponds to the most negative possible coefficient. This condition, as shown in Figure 3.30, occurs especially for the installation position further forward, with the engine entirely installed under the hull. Good results are also obtained for the installation configuration where the inlet is located at the maximum longitudinal coordinate, thus furthest from the hull trailing edge. In contrast, the worst condition corresponds to the intermediate position at the longitudinal coordinate $(-0.7788\ ;\ -0.16576)$, where cavitation occurs.

In the off-design case as well, the best possible condition is the one corresponding to the minimum net force coefficient. Since the Net Vehicle Forces are negative in this case, the optimal configuration is the one for which $|NVF_{installed}| > |NVF_{isolated}|$, or rather when $NVF_{installed} << NVF_{isolated}$.
It can also be observed that the two contour plots are very similar in both values and colours, indicating similar propulsor behaviour under different operating conditions. In Figure 3.31 as well, the same positions are shown to be favourable for installing the propulsor.
However, a slight difference can be observed in the position with longitudinal coordinate $0.271\ ;\ -0.1657$, where a condition of maximum efficiency is found, unlike the design case in which the greatest benefit is obtained exclusively at the $x/D \approx -3.4035$ coordinate.

The described behaviour demonstrates that the most significant benefit of the ODW installation is the reduction of drag on the hull surface. In fact, the best NVF values are obtained in the positions in which the drag on the hull is minimised.

4 CONCLUSIONS

Today's waterjet marine propulsion systems are intrinsically linked to the integration of the propulsion system into the hull, causing performance drops due to flow distortion and losses from the interaction with the hull boundary layer.
The Outboard Dynamic-inlet Waterjet (ODW) solves most of these issues: its installation configuration allows the dynamic intake to be fully immersed in the flow, thus avoiding duct losses caused by wall-fluid friction and recirculation zones that typically form. However, several considerations must be analysed to discover the interactions between the hull and the propulsive system.
The simulations, which are performed by solving the RANS equations in Fluent using the pressure-based method and the k-ω SST turbulence model, have allowed to evaluate the most suitable installation positions and how these affect the characteristic parameters of the propulsor. There is no single installation position that maximises all performance parameters under every operating condition; therefore, it is necessary to perform trade-off analyses to identify the most balanced configuration.

4.1 Summary Results

In this section, the main conclusions are reported.
It is worth noting that most installation points exhibit similar behaviours, with values that improve or worsen depending on the parameter considered. This highlights the need for a careful performance optimisation study.
The first conclusion, based on what was discussed in Section 3.3.1, concerns the cruise condition with $IVR = 0.85$. In this scenario, which is expected to represent the majority of the operational life of the vessel, the propulsion system must ensure maximum efficiency. For this reason, all conditions that could potentially lead to surface damage or component wear should be avoided. Consequently, the installation of the ODW unit at the coordinates $-0.7788\ ;\ -0.16576$ should be excluded because it leads to a double cavitation region at the upper nozzle outlet and at the top edge of the upper intake, which can cause bubbles to collapse, resulting in possible erosion of the propulsor walls or performance.
Pressure coefficient analyses show that a very close installation can lead to undesirable effects, such as sudden variations in C_p along the keel and on the external walls of the propulsion unit, suggesting potential disturbances in free-stream flow, such as small separation bubbles. Although marginal, these effects can lead to a local decrease in performance; the intensity of such effects appears to depend on the coordinate of the longitudinal installation.
Dynamic investigations carried out on the hull revealed that the vertical installation coordinate only marginally affects the drag generated on the hull surfaces, while the longitudinal coordinate plays a significant role. Under both design and off-design conditions, a clear reduction in drag is observed when the unit is positioned further forward, where the performance exceeds that of

the isolated hull. However, the lift generated on the hull in the same installation positions has a negative impact on performance as it increases the downforce, and therefore the wetted surface area of the hull, potentially increasing the hydrodynamic resistance.
The dynamic analysis of the propulsion unit further shows that drag is reduced when the installation is shifted aft. In the best-case scenario, under design conditions, performance improves even compared to the isolated case, suggesting a beneficial interaction between the hull and the propulsion system; the net propulsive force is also maximised in these positions.
In the end, the most important propulsive parameter, the Net Vehicle Force, which considers the effects of the entire submerged domain, shows that the positions where the highest efficiency is reached are characterised by dimensionless longitudinal coordinate $\tilde{x} = -3.4035$, while the vertical coordinates have no particular influence on the obtained results. This trend is also confirmed under low-speed off-design conditions.

This work represents a solid basis for a better understanding of the installation effects on this novel type of waterjet and provides support for future optimisation studies.

4.2 Future developments

Based on the considerations made throughout this work, several additional investigations can be conducted to better define this propulsion system and improve its characteristics.

Potential research directions linked to this project include the following:

- Development and simulation of a planing hull model in which the trim is allowed to change during motion, to which a wave model could later be added. This would allow for a detailed analysis of how different trim conditions affect the propulsor's performance. For instance, a cruise trim with a raised bow would significantly influence the operating conditions of the axial pump, similarly to what occurs in a turbofan during take-off.
- Integration of the axial pump within a fully three-dimensional fluid domain model, including both the hull and the installed propulsion system.
- Application of a multiphase cavitation model within the three-dimensional domain. This study was not carried out because of technical issues in Ansys caused by the three-dimensional nature of the geometry.

BIBLIOGRAPHY

[1] A. ESLAMDOOST, *The Hydrodynamics of Waterjet/Hull Interaction*. PhD thesis, Chalmers University of Technology, 2014.

[2] N. W. H. Bulten, *Numerical Analysis of a Waterjet Propulsion System*. PhD thesis, Technische Universiteit Eindhoven, 2006.

[3] E. B. Andrea Magrini, Denis Buosi, "Maximisation of installed net resulting force through multi-level optimisation of an ultra-high bypass ratio engine nacelle," *Elsevier Masson SAS.*, 2021.

[4] J. Kock, S.Kruger, N. Rensburg, and R.F.Laubscher, "Aerodynamic optimization in light weight solar vehicle design," *Proceedings of the ASME 2014 International Mechanical Engineering Congress and Exposition IMECE2014*, November, 2014.

[5] P. S. Ward, "Bill hamilton, river king." `https://www.nzedge.com/legends/bill-hamilton/`, 23 December, 2005. Accessed: 27 February 2025.

[6] J. Sherwood, "Patrol boat river (pbr) lethality in vietnam." `https://usnhistory.navylive.dodlive.mil/Recent/Article-View/Article/2686264/patrol-boat-river-pbr-lethality-in-vietnam/`, 10 January 2017. Accessed: 27 February 2025.

[7] Università degli Studi di Padova, Università Ca' Foscari Venezia, "SILENZIOSO E SOSTENIBILE, ECCO IMPRONTA-0 IL MOTORE DEL FUTURO PER NAVIGARE A VENEZIA," 10 December 2024. Press release.

[8] A. FILIPPO, *Numerical Methods for Design, Validation and Optimisation of High-Performance Waterjets*. PhD thesis, Univesità degli Studi di Padova, 2024.

[9] T. Giorgio, "Fondamenti e applicazioni di propulsione navale." Università degli Studi di Trieste, Dipartimento di Ingegneria e Architettura, Sezione di ingegneria navale.

[10] *ANSYS fluent 24.2 theory guide*.

[11] CINECA, "Cineca high performance computing." `https://www.hpc.cineca.it`, 2025. Accessed: 3 March 2025.

[12] M. S. Group, *Guide to in-flight thrust measurement of turbo-jets and fan engines*. Agardograph No. 237, Technical Report No. AG-237, AGARD, 1979.

[13] I. P.Canestrelli, S.Vazzoler, "Studio ed ottimizzazione delle carene delle imbarcazioni lagunari," tech. rep., Centro previsioni e Segnalazioni maree, 2003.

[14] S. L. R.W. Wilson, *Shreir's Corrosion*. Elsevier, 2010.

[15] A. F. E.Lee, C. R. Weil, "Experimental results for the calm water resistance of the generic prismatic planing hull (gpph)," tech. rep., Naval Architecture and Engineering Department, NSWCCD, May, 2017.